Nuclear Physics B84 (1975) 3–54. North-Holland Publishing Company

NEUTRON-PROTON CHARGE-EXCHANGE SCATTERING FROM 8 TO 29 GeV/c *

Michael N. KREISLER
Princeton University, Princeton, New Jersey 08540
and
University of Massachusetts, Amherst, Massachusetts 01002 †

Michael B. DAVIS
Princeton University, Princeton, New Jersey 08540
and
Carnegie Institution of Washington, Washington, DC ††

Michael J. LONGO and Donald D. O'BRIEN ‡
University of Michigan, Ann Arbor, Michigan 48104

Received 8 August 1974
(Revised 16 September 1974)

Abstract: The differential cross sections for neutron-proton charge-exchange scattering have been measured for incident neutron momenta between 8 and 29 GeV/c and for four-momentum transfers $|t|$ between 0.002 and 1.0 (GeV/c)^2. A neutron beam with a broad momentum spectrum was scattered from a liquid hydrogen target. The momenta and scattering angles of the forward-scattered protons were measured by a spark-chamber magnet spectrometer. The flight times and scattering angles of the recoil neutrons were measured by a bank of thick scintillation counters. The efficiencies of the neutron counters were determined in a separate measurement. Absolute normalization of the data was obtained from a measurement of the diffraction dissociation of neutrons from carbon nuclei. Differential cross sections, based on ~ 23 000 events, are presented for 9 different momenta. The shape of the differential cross sections and the momentum dependence are examined in detail.

1. Introduction

In this paper, we describe an experiment to measure the differential cross section for neutron-proton charge-exchange scattering,

* Work supported by the US Atomic Energy Commission and the US National Science Foundation.
† Permanent address.
†† Present address.
‡ Present address: McGill University, Montreal, Quebec, Canada.

$$n + p \rightarrow p + n .$$

The experiment, performed at the Brookhaven Alternating Gradient Synchrotron, used a neutron beam containing neutrons with momenta between 8 and 29 GeV/c. Preliminary reports [1–3] of this work have been published elsewhere.

Previous experiments [4–12] indicated that this process has several interesting characteristics. There is a peak in the angular distributions which is much sharper than the peak in p–p scattering. This peak appears in data with energies ranging from below the one-pion threshold up to the highest energies studied. The distributions in t, the square of the four-momentum transfer between the incoming neutron and the outgoing proton, appear to be essentially independent of energy above 1 GeV, and the integrated cross section decreases with increasing energy.

The general shape of the cross section at 3 GeV/c [4, 5] can be described by

$$d\sigma/dt = A\, e^{-B|t|} + C\, e^{-D|t|} ,$$

where $B \approx 50\,(\mathrm{GeV}/c)^{-2}$, $D \approx 4\,(\mathrm{GeV}/c)^{-2}$, and $A \approx C$. B, the slope of the more rapidly varying term, is approximately equal to $1/m_\pi^2$ (m_π = mass of pion), which suggests that the peak is due to one-pion exchange. However, a simple one-pion exchange model predicts a dip at $t = 0$ rather than a peak. In order to explain the peak, more complicated models have been suggested. Data at higher energy and larger values of $|t|$ became necessary to check the predictions of these models.

This experiment was part of a general program to study neutron interactions at high energies. The objectives of the present experiment were the following:

(a) To study the energy dependence of the shape of the differential cross section for n–p charge-exchange scattering; in particular, to determine whether or not there was "shrinkage" of the peak in the angular distributions.

(b) To study the energy dependence of the absolute cross sections by taking measurements over a wide energy range at one time. Previous measurements [4–8] indicated that the cross sections decreased with increasing incident neutron momentum as p_{lab}^{-2} to p_{lab}^{-3}. This experiment, with data taken over a wide energy range with consistent normalization, would give accurate information on the energy dependence of the absolute cross sections.

(c) To extend measurements to larger four-momentum transfers and higher energies than previous experiments.

The method used in this experiment was as follows. A beam containing neutrons with momenta between 8 and 29 GeV/c struck a liquid hydrogen target. The momenta and scattering angles of the forward-scattered protons were measured in a spark-chamber spectrometer. The recoil neutrons were detected by a bank of scintillation counters, and their flight times and scattering angles were measured. Kinematic information from the neutron and proton arms were compared to determine which events were elastic. The neutron flux was measured in a separate experiment in the same beam line.

In the sections that follow, we present a detailed discussion of our experiment and summarize previous work on this process.

2. Summary of previous experimental and theoretical work

2.1. Kinematics

The variables used to describe the kinematics of the n–p charge-exchange reaction

$$n + p \rightarrow p + n$$

$$1 + 2 \rightarrow 3 + 4,$$

are shown in fig. 1, where $\vec{p}_i$ represents the three-momentum and P_i the four-momentum of particle i. The quantities s, t and u represent, respectively, the c.m. energy squared, the four-momentum transfer squared between particles 1 and 3, and

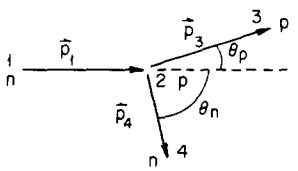

(a) Laboratory System

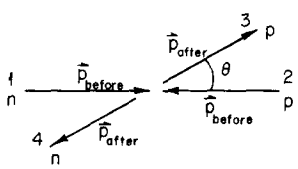

(b) Center of Mass System

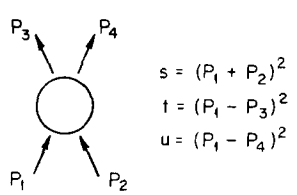

(c) Mandelstam Variables

$1 + 2 \rightarrow 3 + 4$

$n + p \rightarrow p + n$

Fig. 1. Kinematic variables for the reaction n + p → p + n.

the four-momentum transfer squared between particles 1 and 4. If the neutron-proton mass difference is neglected and $c \equiv 1$,

$$s = 2m^2 + 2mE_{\text{lab}} \simeq 2mp_{\text{lab}} ,$$

$$t = -2mT_{\text{n}} \simeq -p_{\text{lab}}^2 \theta_{\text{p}}^2 ,$$

where p_{lab} and E_{lab} are the incident neutron momentum and energy; T_{n} is the final neutron kinetic energy; and θ_{p} is the laboratory scattering angle of the proton. In this paper the n–p scattering reaction will generally be described by its values of p_{lab} and t.

2.2. Summary of previous experimental data

Neutron-proton charge-exchange differential cross sections have been measured at high energies using the following three experimental methods.

(i) The double charge-exchange method. A neutron is produced in a deuterium or beryllium target by elastic p–n charge-exchange. The neutron in turn undergoes elastic n–p charge-exchange scattering in a second liquid hydrogen target. The scattered proton is required to have the full beam energy to ensure that two successive charge-exchange reactions have taken place; the scattered neutron is not detected. An advantage of this method is that the angular distributions can be measured to $t = 0$. However at high energies extremely good momentum resolution is necessary to separate the protons which have undergone double charge-exchange scattering from those which are inelastically produced. Also, in order to normalize the cross sections it is necessary to know the effective number of free neutrons contributing to the p–n charge-exchange reaction in the primary target, a number which is difficult to determine accurately.

(ii) The incident neutron time-of-flight method. A neutron beam with a broad momentum spectrum is used. The energies of the incident neutrons are determined from their flight times, and the momenta of the forward-scattered protons are measured; the recoil neutrons are not detected. With this method it is not necessary to require double charge exchange; momentum resolution is therefore less critical than in the first method. A disadvantage of this technique is that it can be used only at low energies where the neutron energy can be determined from the flight time.

(iii) The recoil neutron time-of-flight method. A neutron beam with a broad momentum spectrum is used, and the momentum vectors of both particles in the final state are measured. Inelastic events can be separated from elastics because the kinematics of each event is overdetermined. A disadvantage of this method is that the efficiencies of the neutron counters must be determined. Because the efficiencies are low at neutron kinetic energies below 1 MeV, it is difficult to measure the differential cross sections for $-t < 0.002\ (\text{GeV}/c)^2$. This method was first employed by Powell et al. at the Bevatron [6].

The first measurements of neutron-proton charge-exchange scattering above 2 GeV were made in 1962 by Palevsky et al. [4], who measured the differential cross sections at incident neutron momenta of 2.83 GeV/c and 3.67 GeV/c. The double charge-exchange method was used, and the velocity of the final proton was measured in a threshold gas Čerenkov counter. It was found that the distributions in transverse momentum $p_\perp = p_0 \sin\theta \simeq \sqrt{-t}$ were the same for both energies; that the distributions were sharply peaked at zero momentum transfer, falling to half maximum at $p_\perp = 150$ MeV/c; and that at $p_\perp = 0$ cross sections were an order of magnitude smaller than the forward p–p cross sections.

In 1965, using the same technique, the same group [5] measured the differential cross sections at 3 GeV/c and the $p_\perp = 0$ cross sections at 1.40, 2.35 and 2.55 GeV/c. They compared the shapes of their cross sections with the data of Larsen [7] at 1.37 GeV/c and the preliminary data of Manning et al. [8] at 8.15 GeV/c. The shapes appeared to be the same for all energies studied, with slight evidence for a narrowing of the peak at the higher energies. It was found that the angular distributions at 3 GeV/c could be fit rather well by the two-exponential form

$$d\sigma/dt\ [\mathrm{mb/(GeV/}c)^2] = 6.9\, e^{-49|t|} + 4.1\, e^{-4|t|}\ .$$

The logarithmic slope at small $|t|$, 49 $(\mathrm{GeV}/c)^{-2}$, was much larger than that for p–p scattering ($\sim 7\ (\mathrm{GeV}/c)^{-2}$) or $\bar{\mathrm{p}}$–p scattering ($\sim 15\ (\mathrm{GeV}/c)^{-2}$). At larger $|t|$, the cross sections decreased exponentially with a slope of approximately $4\,(\mathrm{GeV}/c)^{-2}$. The $t = 0$ absolute cross sections (including the data of Larsen and the preliminary data from Manning et al.) were found to decrease with increasing incident momentum approximately as p_{lab}^{-2}. The data of Manning et al., however, seemed to indicate that the cross sections might be decreasing as rapidly as p_{lab}^{-3}.

In 1965, Wilson [13] pointed out that the sharp forward peak observed by Palevsky et al. was also a feature of lower energy cross sections. He examined the t dependence of n–p charge-exchange cross sections at energies from 91 MeV to 2.85 GeV and concluded that the momentum transfer distributions were essentially the same for all energies.

In 1966 Manning et al. [8] published the results of a measurement of the n–p charge-exchange cross section at 8 GeV/c. They used the double charge-exchange method and measured the proton momentum in a spark chamber spectrometer. Comparing their results with those at lower energies, they found that for small $|t|$, the shape of the cross sections seemed to be independent of energy. For $-t > 0.1\ (\mathrm{GeV}/c)^2$, however, the ratio $[(d\sigma/dt)/(d\sigma/dt)_{t=0}]$ at constant t seemed to decrease with increasing energy. They also found that the $t = 0$ cross section continued to decrease rapidly with increasing energy.

In 1969, Mischke et al. [9] measured n–p charge-exchange cross sections between 0.6 and 2.0 GeV/c, using the second of the three methods described above. The cross sections showed a sharp change in slope around $-t = 0.01\ (\mathrm{GeV}/c)^2$. Near $t = 0$ the logarithmic slopes varied from approximately $100\ (\mathrm{GeV}/c)^{-2}$ at the lowest

energies to approximately 30 $(\mathrm{GeV}/c)^{-2}$ at the highest energy, a more complicated behavior than had been previously observed. At larger values of $|t|(>0.02\,(\mathrm{GeV}/c)^2)$, the slope was approximately 6.5 $(\mathrm{GeV}/c)^{-2}$, independent of energy.

In 1971, Miller et al. [10, 11] measured n–p charge-exchange cross sections from 3 to 12 GeV/c, using the third method described above. They found a sharp peak in the differential cross sections with a slope of approximately 50 $(\mathrm{GeV}/c)^{-2}$ and a slower exponential fall-off at larger $|t|$ with a slope of approximately 5 $(\mathrm{GeV}/c)^{-2}$. The shapes of the cross sections were essentially energy independent. The $t = 0$ cross sections decreased with increasing energy as $p_{\mathrm{lab}}^{-2.1}$.

In the same year, Engler et al. [12] made measurements of n–p charge-exchange differential cross sections at 8, 19.2 and 24 GeV/c, using the double charge exchange method. They found that the peak in the cross section persisted to 24 GeV/c and that the t dependence of the cross section did not change appreciably with energy. The $t = 0$ cross sections had an energy dependence consistent with p_{lab}^{-2}.

Measurements of the polarization in n–p charge-exchange scattering between 1 and 12 GeV/c have also been made using method (iii) [14].

2.3. Summary of theoretical work

The observation of a sharp peak in n–p charge-exchange cross sections, with a width approximately equal to m_π^2, has led to many attempts to explain the peak in terms of a pion pole. In 1958 Chew [15] pointed out that the real part of the n–p scattering amplitude should have a pole in the non-physical region at $t = m_\pi^2$. He suggested that the data from n–p scattering experiments (backward or forward scattering) could be extrapolated to the pion pole to determine the pion-nucleon coupling constant. Several groups [7, 16–18] performed this extrapolation at energies between 300 and 800 MeV and found values for the coupling constant which agreed with the values found from π–N scattering. This result strongly suggested that one-pion exchange contributed to n–p scattering at small angles.

The cross section obtained from one-pion exchange in the first Born approximation is

$$\frac{\mathrm{d}\sigma}{\mathrm{d}t} \propto \left(\frac{t}{t - m_\pi^2}\right)^2 .$$

This cross section obviously goes to zero at $t = 0$. Since the observed peak cannot be explained by one-pion exchange alone, it is possible that other particles are exchanged. Possible candidates which satisfy the necessary conservation laws are the π, ρ and A_2.

There were several attempts to fit the data with simple π and ρ exchange models [19–22]. Phillips [19] showed that the sharp peak could be explained as the strong interference between a one-pion exchange term and a slowly varying background from other processes (put in phenomenologically). Muzinich [20] suggested the exchange of a reggeized ρ. It was later shown [23], however, that ρ exchange alone

could not explain simultaneously the energy dependence of the differential cross section $d\sigma/d\Omega$ ($t = 0$) and the magnitude of the cross section difference $\sigma_T(pp) - \sigma_T(np)$. Islam and Preist [21] suggested the exchange of both ρ and π, with the sharp peak due to a rapidly decreasing form factor for the ρ exchange. Bugg [24] gave a possible explanation for the peak in terms of the difference between diffraction scattering in the isotopic spin $T = 0$ and $T = 1$ channels. Glück [22] suggested the exchange of a π^+ in the t-channel and a π^0 in the u-channel, the shape caused by interference between the two contributions.

Some of the early papers [17, 19] had considered the interference of the pion pole term with a slowly varying background amplitude (chosen phenomenologically). This idea was further developed by including corrections for absorption effects caused by competing inelastic channels in the initial and final states. As Gottfried and Jackson [25] pointed out, competing inelastic channels would be most effective at small impact parameters (i.e., in low angular momentum states) and would therefore reduce the low partial-wave amplitudes below the values given by the one-particle-exchange model leaving the higher partial wave amplitudes essentially unchanged. The result would be a reduction in the reaction cross section and collimation of the angular distributions in the small t direction. Several theorists [26–28] calculated simple π and ρ contributions to n–p charge exchange and then included corrections for absorption of each partial wave, based on the parameters found from p–p scattering. The one-pion-exchange model with absorption gave reasonable agreement with experiments for $-t < 0.01$ $(\mathrm{GeV}/c)^2$ but predicted a secondary maxima in the cross sections which was not observed. Absorption models also could not explain the persistence of the forward peak to very low energies (below inelastic thresholds). However, it was pointed out [29] that perhaps the elastic unitarity requirement modifies the lower partial waves at low energy in the same way that absorption does at high energy.

Another model combining one-pion exchange with absorptive effects was the "coherent droplet" model of Byers and Yang [30], which Byers applied to n–p charge exchange scattering. In this model, scattering in high angular momentum states (large impact parameters) was dominated by one-pion exchange. Scattering at small impact parameters was pictured as the passage of one extended object through another, with resulting absorption. This model was able to fit the shapes of both $np \to pn$ and $\bar{p}p \to \bar{n}n$ cross sections.

There have been many attempts to explain the s and t dependence of the n–p charge exchange cross sections using Regge theory. The differential cross section (at small $|t|$) for a process dominated by a single Regge exchange can be written [31]

$$\frac{d\sigma}{dt} = F(t)\left(\frac{s}{s_0}\right)^{2\alpha_0 - 2} e^{2\alpha' \ln(s/s_0)t},$$

where $F(t)$ accounts for all the t dependence which is not included in the last term; $\alpha' \simeq 1$ $(\mathrm{GeV}/c)^{-2}$, and $\alpha_0 \simeq 0$, 0.5 and 0.5 for π, ρ and A_2 respectively; and s_0 is a scale factor usually taken to be 1 GeV^2. This equation makes three predictions about the energy dependence of the cross section:

(a) The angular distributions will "shrink" (become more peaked near $t = 0$) with increasing energy.

(b) At $t = 0$, the differential cross section will decrease with energy as s^{-2} if pion exchange ($\alpha(0) \simeq 0$) dominates and as s^{-1} if ρ or A_2 exchange ($\alpha(0) \simeq 0.5$) dominates.

(c) Apart from shrinkage, the t dependence (at small $|t|$) of the cross sections will be independent of energy.

The simple one-Regge exchange model fits the energy dependence of the n–p charge exchange cross sections. Present data indicates that there is no shrinkage. To explain the t dependence of the cross sections, however, more complicated models are necessary. Before discussing these models it is useful to list the features of n–p scattering data which, as Arbab and Dash [32] have pointed out, must be explained by any successful theory. These features are:

(a) the sharp peak in $np \to pn$, with width $\simeq m_\pi^2$,

(b) the fact that the peak persists to very low energies and is almost energy independent,

(c) the large difference in the magnitudes of the cross sections for $np \to pn$ and for $\bar{p}p \to \bar{n}n$ at the same value of s and t (for $|t| > 0.02$ (GeV/c)^2),

(d) the energy dependence of the $\bar{p}p \to \bar{n}n$ data (due to crossing symmetry). In addition any theory must explain the polarization data now available.

Because the pion contribution vanishes at $t = 0$, early Regge models did not include pion exchange. Using ρ and A_2 exchange, Ahmadzadeh [33] was able to explain simultaneously the energy dependence of $d\sigma/d\Omega$ ($t = 0$) and the magnitude of $\sigma_T(pp) - \sigma_T(np)$; he made no attempt to determine the t dependence of the cross sections. Flores-Maldonado [34], also using ρ and A_2 exchange, was able to fit the differential cross sections for $np \to pn$ and for $\bar{p}n \to \bar{n}p$ but was not able to explain requirement (c) above. There were several objections to models which did not include the pion contribution. For example, the small observed values of $\sigma_T(pp) - \sigma_T(np)$ are consistent with small contributions from the ρ and A_2 at $t = 0$ rather than with the large values required by the above models [32].

With the advent of "conspiracy" [35], several mechanisms were suggested through which the pion could cause a sharp peak in the cross section near $t = 0$. It was shown [32, 36] that if there exists a conspirator to the pion, with the quantum numbers of the pion but with positive parity, then it is not necessary for all the pion amplitudes to vanish at $t = 0$. Phillips [36] and Arbab and Dash [32] used a pion conspirator and various other combinations of Regge exchanges (including the ρ and A_2) to fit the $np \to pn$ and the $\bar{p}p \to \bar{n}n$ data. The fits to the $\bar{p}p \to \bar{n}n$ data were not very good. Several other papers [37–39] have also used conspiracy in fitting n–p charge-exchange cross sections.

There have been many objections to the conspirator model. One objection is that a conspirator to the pion is rather artificial, since no particle has been observed which would correspond to the pion conspirator. LeBellac [40] has also shown that the existence of a pion conspiracy leads to incorrect predictions about other reactions.

Recent Regge models [41–47] have considered the effects of absorption or rescattering (these show up mathematically as cuts). One such model is the "strong cut Reggeized absorption model" [43–45] (SCRAM), which has the following physical interpretation. Since the front part of a particle can shadow the rear part, the probability that a reaction will occur in which a particle is exchanged in a head-on collision is decreased from its value assuming no shadowing. If the strength of the shadowing is increased compared to estimates based on elastic scattering, there will be a strong suppression of reactions with small impact parameters, leading to diffractive effects. The SCRAM model superimposes these strong absorption effects on a smooth Regge pole amplitude [44].

In the Regge cut models [41–47] the peak in n–p charge-exchange scattering is caused by the interference of a pion pole and one or more cuts. These cuts are generated in different ways by the different models. All these models have been successful in fitting the shape and energy dependence of the cross sections at small $|t|$ but have had differing amounts of success at large values of $|t|$. More complicated models will probably be able to improve the fits at large $|t|$. The model of Gotsman and Maor [46], which suppresses the pion contribution for $-t \geqslant 0.2$ (GeV/c)^2, gives rather good fits at both small and large $|t|$.

Two other recent fits to n–p charge-exchange scattering data should be mentioned here. Engler et al. [48] was able to get reasonable fits to np → pn data and $\bar{p}p \to \bar{n}n$ data by considering the interference between a Reggeized pion and a phenomenologically chosen background. Lusignoli and Srivastava [49] were able to get good fits to the n–p charge-exchange cross section using a model in which a ρ and A_2 were exchanged in the t channel and a π was exchanged in both the t and the u channels.

The Regge cut models have been quite successful in fitting a large number of different reactions, including n–p charge exchange. Our data will be compared with some of these models later in this paper.

3. Experimental equipment and procedure

The measurement of the n–p charge-exchange process utilized a neutron beam derived at 0° from a Be target in the AGS slow-extracted proton beam. The neutrons, with momenta between 8 and 29 GeV/c, bombarded a liquid hydrogen target. The forward-scattered protons from the charge-exchange reaction were detected by three proton counters, and their scattering angles and momenta were measured in a spark-chamber magnet spectrometer. The recoil neutrons, with kinetic energies of 1 to 500 MeV, were detected by a bank of fifteen scintillation counters, and their scattering angles and flight times were measured. Information about each event was recorded on magnetic tape, and was also transmitted to an on-line computer where a preliminary analysis was done. The details of this measurement are discussed below.

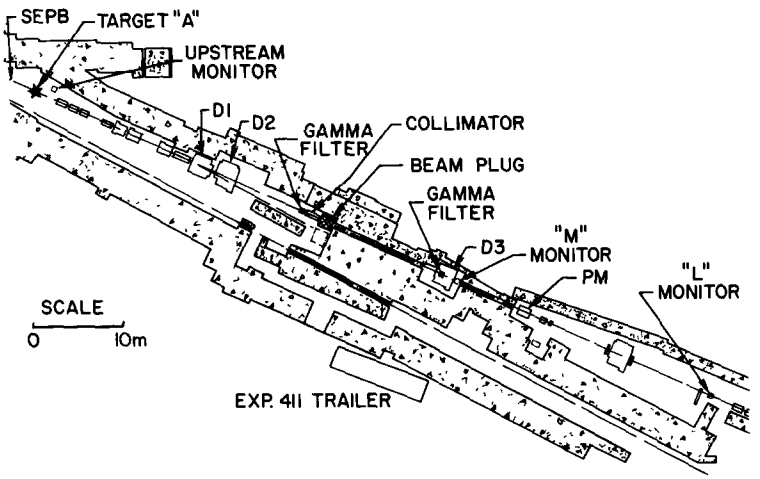

Fig. 2. Beam line.

3.1. Beam line

A sketch of the beam line is shown in fig. 2. The slow extracted proton beam, with an intensity $\sim 2 \times 10^{11}$ protons per pulse and at a beam momentum of 28.5 GeV/c, was steered onto a Be target (target "A") 0.25 cm high by 0.51 cm wide by 18.0 cm long (0.6 collision lengths). A neutral beam was taken off at 0° relative to the incident beam. Charged particles were swept horizontally out of the beam by dipole magnets D_1, D_2, D_3 and vertically by pitching magnet PM. The proton beam was stopped in a beam dump consisting of 1.2 m of lead and approximately 25 m of heavy concrete. The deflection of the proton beam in the sweeping magnets was sufficient to prevent large muon fluxes from reaching the main experimental area. Gamma rays were converted by 4.2 radiation lengths of lead and the charged particles produced were eliminated by the sweeping magnets. Contamination of the neutron beam by gammas was less than one percent; contamination by kaons was negligible.

The size of the neutron beam was defined by a 91 cm long brass collimator with a 1.43 cm diameter hole, located 32 m downstream from the target. The beam halo was reduced by oversize collimators in magnets D_3 and PM. At the position of the liquid hydrogen target, 59 m downstream from target A, the beam was circular, 2.54 cm in diameter, with negligible halo. Detailed position and shape information of the neutron beam was obtained periodically with a film holder containing a thin converter, a scintillator screen, and a Polaroid film placed in a surveyed position in the beam line. Uniformity of the beam spill was monitored by a small lucite Čerenkov counter located near the production target.

The beam subtended a solid angle of 1.55×10^{-7} sr at the production target and

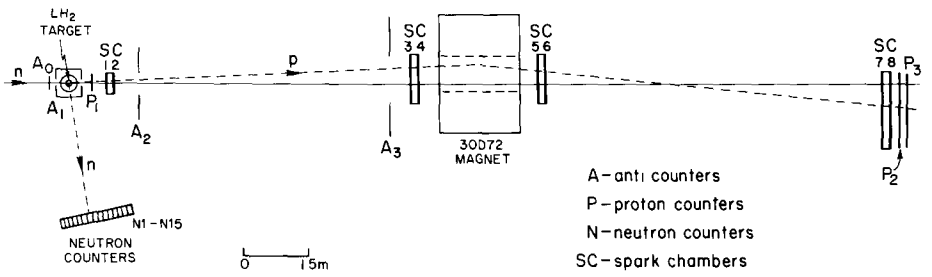

Fig. 4. Experimental layout.

3.2. Liquid hydrogen target and anticounters

The liquid hydrogen target (LH_2), shown in fig. 3, was a 7.6 cm diameter cylinder with its axis vertical. It was made of 0.19 mm mylar and wrapped with 4 layers of 6.4 μm superinsulation. The target was enclosed in a 1.22 mm cylindrical aluminum vacuum jacket with 3.2 cm diameter mylar windows 0.25 mm thick for the beam. The neutron beam was attenuated by approximately 2% in passing through the target.

The target was almost completely surrounded by an anti-counter arrangement as shown in fig. 4. The beam anti, A_0, was 0.16 cm thick and ensured a neutral incident particle. A_1 (0.32 cm thick) shielded the neutron counters from charged particles emerging from the target. The rest of the anti array consisted of a sandwich of lead and scintillator in order to veto gammas as well. The "baffle" counters A_2 and A_3, preceded by 0.65 cm plates of lead, detected particles which escaped through the hole in the downstream end of the anti-counter box surrounding the target.

The anticounters vetoed approximately 9 out of every 10 proton candidates. Approximately 5% of the good events were vetoed due to accidentals in the anticounters.

3.3. The proton spectrometer

The layout of the arm of the spectrometer used to detect the outgoing proton is shown in fig. 4. The magnet was 76.2 cm wide by 1.83 m long with a 15.2 cm gap. There were three scintillation counters which were part of the trigger requirement: P_1, 0.32 cm thick, located 76 cm downstream of the LH_2 target; and P_2 and P_3, each 1 cm thick, located $\sim$ 13 cm downstream of the last chamber. Since P_1 determined the timing for the event, its signal was kept short with a 3 nsec clipping line. Relative timing between the neutron counters and the proton arms was set using nanosecond light pulsers attached to each counter. This pulser arrangement is discussed below.

The spectrometer consisted of eight wire spark chambers, four on each side of the magnet. The chambers on each side of the magnet were placed in two sets of two chambers each, with a separation between the sets of about 7.6 m.

Helium bags were placed between the sets of chambers in order to reduce multiple Coulomb scattering of the protons. The total material between the LH_2 target and the center of the magnet was 1.6 g/cm^2 (0.039 radiation lengths) and the total material between the center of the magnet and the last spark chamber was 0.8 g/cm^2 (0.016 radiation lengths). The angular uncertainty in the proton direction due to material in the hydrogen target and the first proton counter was approximately 0.05 mrad at 25 GeV/*c*.

Each of the wire spark chambers consisted of orthogonal wire planes expoxied to opposite sides of a 1 cm fiberglass frame. The spacing between wires (0.18 mm diameter aluminum) was 1 mm. A sheet of 0.08 mm mylar was glued over each side of the frame with RTV Silastic cement. A mixture of 90% neon and 10% helium flowed in the gap at a pressure slightly above atmospheric.

The chambers were attached to aluminum frames which supported them and contained the high voltage connections. Two chambers were attached to each 5 cm thick frame, one on each side. One chamber in each set had wires running horizontally and vertically, and the other chamber had wires at 45° and 135°. The use of two chambers with different wire orientations helped to resolve ambiguities in spark positions when there was more than one spark in a chamber.

The chambers were pulsed at about 10 kV by a set of spark gaps and capacitors. A dc clearing field of 50 V was applied to the chambers. A 25 msec dead time after each trigger allowed the spark chambers to recover. In order to improve the propagation of the high voltage pulse, an aluminum foil, insulated by a mylar sheet, was placed next to each high voltage plane and connected to the high voltage.

The active areas of the chambers were as follows: 17.8 cm by 29.8 cm for chambers SC1 and SC2, 24.1 cm by 81.3 cm for SC3 and SC4, and 40.6 cm by 1.17 m for SC5, SC6, SC7 and SC8. The net mass per chamber was 0.042 g/cm^2.

Spark positions were determined from magnetostrictive delay lines attached to aluminum "wands" with a MIDAS digitizing system (Science Accessories Corporation) [50], capable of digitizing two sparks for each of the sixteen delay lines (one delay line for each wire plane). Uncertainties in the spark positions were less than 1 mm.

The chambers closest to the magnet operated in fields of 100 to 200 G. The delay lines for these chambers were shielded with 1 cm thick soft iron plates. Extraneous noise pickup in the preamplifiers was reduced by a common ground between all preamplifiers and the spark gaps.

The analyzing magnet was a BNL 30D72. The magnet was run at two currents, 2020 A and 1340 A. The lower setting was used to increase the acceptance for low momentum protons. A magnet of this type had been completely mapped by the AGS Magnet Measurements Group. At the time of the experiment, the field was measured at 200 points and at several different current settings with a Hall probe which had been calibrated against a nuclear magnetic resonance probe. These measurements agreed to better than 0.5% with those taken by the Magnet Measurements Group. The fields at the center of the median plane were 18.00 kG and 12.22 kG at

2020 A and 1340 A respectively. The corresponding field integrals along the center line of the magnet were 1416 kG in and 977 kG in, with uncertainties of less than 0.5%.

Fringe fields extended into the region beyond the spark chambers closest to the magnet. The field integral in the region beyond the chambers was less than 0.1% of the total $\int \boldsymbol{B} \cdot \mathrm{d}\boldsymbol{l}$.

Two kinds of special runs were made in order to check the alignment of the chambers: runs with the surveyed center wires of each chamber pulsed (using no beam), and "straight-through" runs with the magnet turned off. After small alignment corrections were made, the scattering angles of the proton were determined to better than 0.2 mrad, which corresponds to a position uncertainty in each chamber of approximately 1 mm. The proton momentum was measured to better than 0.8% at 25 GeV/c.

The efficiency of the chamber system was approximately 98.5%. Details of the efficiency measurement and its effect on the results are presented later.

3.4. The neutron arm

The recoil neutrons, with energies of 1 MeV to 500 MeV, were detected by a bank of 15 scintillation counters, N_1–N_{15}, which subtended the angular region from 60° to 90° with respect to the incident neutron beam. The neutron counters, shown in fig. 5, were lucite boxes 10.2 cm deep by 5.1 cm wide by 1.22 m high, filled with a mixture of mineral oil and scintillator which is described elsewhere [51]. It was necessary to have the counters as deep as possible to improve the detection efficiency but as thin as possible to improve the timing resolution. The depth of 10.2 cm was a compromise between these two requirements. The centers of the counters were roughly 2.39 m from the target. Uncertainties of ± 5 cm in the neutron interaction position because of the counter depth therefore caused uncertainties in the neutron time of flight of approximately 2%. Three sides of each counter were made of 0.63 cm lucite. The fourth side, the neutron entrance face, was 0.32 cm lucite. The counters were mounted vertically, 7.6 cm apart center-to-center. They were in a straight line, with the center counter being 2.39 m from the target. Each counter was rotated so that it faced the target. Each counter was viewed from opposite ends by two RCA 8575 photomultiplier tubes coupled to the scintillator by 15 cm long UVT lucite light pipes. Relative timing between the two photomultipliers determined the position of the neutron interaction in a counter to ± 5 cm.

The efficiency of each counter depended on the light collection threshold, which was a function of the light collection efficiency of the counter, the gain of the photomultipliers, and the discriminator levels. To facilitate setting and checking the thresholds, a 0.8 mm lucite window was provided on the back of each counter. A calibrated beta source (~ 100 μCi of ^{90}Sr) was placed over the window and the singles rate of each photomultiplier was measured. Frequent adjustments (at least once per day) of the voltages of the photomultipliers were made to keep the singles rates

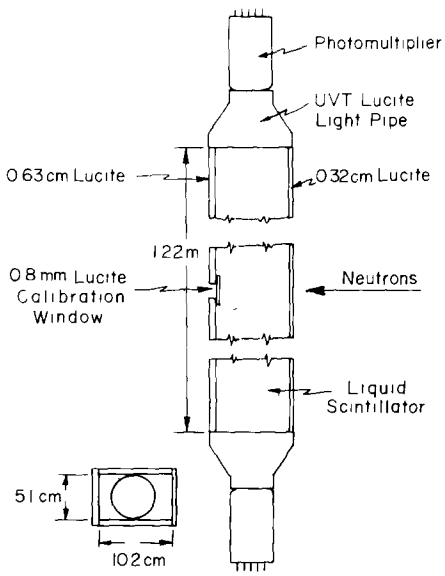

Fig. 5. Neutron counter.

(and therefore the gains) constant over the course of the experiment. Changes in gain corresponding to changes in the photomultiplier high voltage of less than one volt were corrected. Rate-dependent fluctuations in gain were minimized by using high current bases (3 mA) and by stabilizing the voltages on the last three dynodes of the photomultipliers with external power supplies.

Thresholds for the neutron counters were originally set by measuring the maximum pulse height observed in the counter from a ^{90}Sr source, which emits betas with a maximum energy of 2.2 MeV. This was used to estimate the high voltage required to give a threshold for neutrons of the desired energy [52]. The exact thresholds were then determined in a separate experiment as described below. After the photomultiplier gain was set to the proper value, the singles rate was measured and that value of the singles rate was used to set the gain of the counter in all future running. The gain for each counter was determined by the energy of the lowest energy neutron in the angular range of that counter. Table 1 lists the angular, energy, and time of flight ranges of each of the neutron counters, as well as information on the threshold settings.

The efficiencies of the neutron counters were measured in a separate experiment at the Princeton University AVF Cyclotron using the reaction

$$d + d \rightarrow {}^3He + n\,.$$

A beam of "tagged" monoenergetic neutrons for calibrating the counters was pro-

Table 1
Angular, energy, and TOF ranges for the neutron counters

Counter	Scattering angle with respect to the beam (degrees)	Neutron kinetic energy (MeV)	TOF (nsec)	Average TOF (nsec)	Minimum energy β detectable (MeV)	Counting rate with standard ^{90}Sr source (kHz)
1	85.8 – 88.8	1 – 7	66 – 226	146	0.19	300
2	84.0 – 87.0	1 – 17	43 – 203	123	0.24	250
3	82.3 – 85.3	8 – 30	33 – 63	47	0.44	188
4	80.5 – 83.5	18 – 47	27 – 43	34	1.01	75
5	78.6 – 81.6	30 – 68	23 – 33	27	1.01	75
6	76.8 – 79.8	46 – 94	20 – 28	24	1.01	75
7	75.0 – 78.0	64 – 123	18 – 24	20	1.01	75
8	73.2 – 76.2	88 – 157	16 – 21	18	1.01	75
9	71.4 – 74.4	115 – 196	15 – 18	16	1.01	75
10	69.5 – 72.5	146 – 234	14 – 17	15	1.01	75
11	67.7 – 70.7	190 – 290	13 – 15	14	1.01	75
12	65.9 – 68.9	230 – 350	12 – 14	13	1.01	75
13	64.1 – 67.1	270 – 400	12 – 13	12	1.01	75
14	62.4 – 65.4	320 – 470	11 – 12	11	1.01	75
15	60.6 – 63.6	400 – 540	11 – 12	11	1.01	75

duced by identifying the ^{3}He. A detailed description of the calibration procedure has been published elsewhere [53]. The efficiencies were measured to an accuracy of approximately 5% over most of the $|t|$ range. Corrections were made to include the effect of additional neutrons which were scattered into each counter from the 0.63 cm lucite walls of the counter and from adjacent counters. These corrections, calculated by Monte Carlo techniques, varied from 6% of the measured efficiency at small $|t|$ to 12% at large $|t|$, with uncertainties of approximately 3% of the measured efficiency. For completeness, we present a typical efficiency curve in fig. 6..

Since neutron interactions in the scintillator produce a large range of pulse heights, the pulse height for each neutron interaction was measured in order to improve timing resolution. The outputs of the last dynode of the photomultiplier on the bottom of each counter were "daisy chained" together in two groups, and the signals were sent to an analog-to-digital converter. Diodes prevented "cross-talk" between counters. The neutron counter array was enclosed on all sides except the side facing the target by several meters of concrete, lead, and paraffin. The neutron counter cave had a roof of concrete blocks several meters thick.

The timing of the neutron counters relative to the proton counters and the timing of the upper end of each counter relative to the lower end was set with a nanosecond light pulser system (Pek Labs [54]). A pulser was attached to each proton counter and to the center of each neutron counter. Light pulser runs were taken frequently during the experiment to check for drifts in timings. After corrections for drifts were made, uncertainties in neutron time of flight were approximately

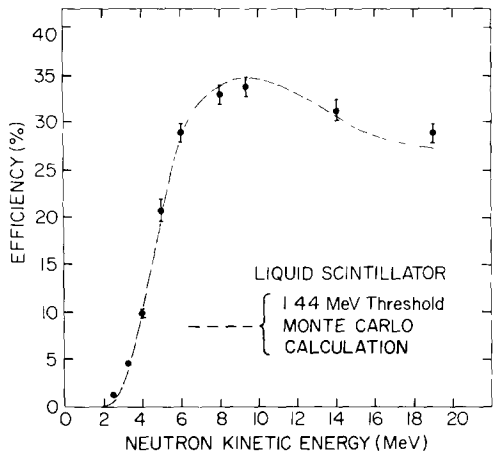

Fig. 6. Efficiency of typical neutron counter (N_4). The dashed line is the result of a Monte Carlo calculation of the efficiency.

± 2.5 nsec for counters N_1 and N_2 and approximately ± 1.5 nsec for counters N_3-N_{16}. Uncertainties in timing between the two ends of a counter were less than 1 nsec, giving updown position uncertainties of approximately ± 5 cm.

Several types of measurements were made with the Pek lamps. A rough calibration was made of ADC readings of the pulse area reading from the last dynode *versus* anode pulse height for each counter (as observed on an oscilloscope). Timing differences between the ends of each counter were measured as a function of pulse height; as expected, pulse height had little effect on these timing differences. Because of the limited range of pulse heights available from the Pek lamps, it was not possible to use the lamps to study the dependence of the measured flight time on the neutron counter pulse height. Such dependence was investigated with the data as will be discussed below.

The relationship between the position of an interaction in a neutron counter and the timing difference between the ends of the counter was found with a series of calibration runs. A 1.2 m long, 1.3 cm diameter scintillation counter was placed 2.5 cm behind the neutron counter array at various heights. A block of paraffin was placed in the beam line at the position of the hydrogen target to produce charged particles. The trigger consisted of the counter A_1 between the target and the neutron counter array, both ends of a neutron counter, and the special counter. These runs calibrated the position measurements and yielded information on the speed of light propagation in the counters.

3.5. Electronics

A simplified block diagram of the logic is shown in fig. 7. Signals from the anodes

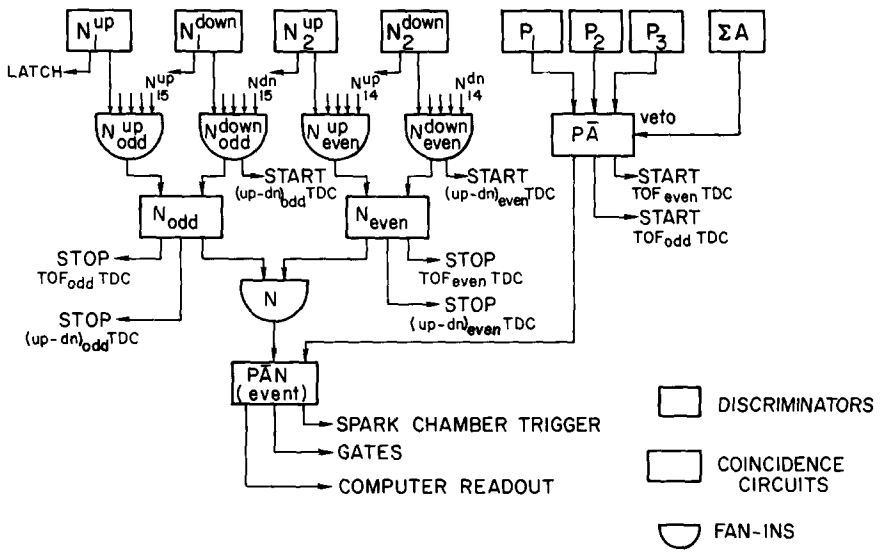

Fig. 7. Simplified logic diagram.

of the photomultipliers at each end of the fifteen neutron counters were brought to Chronetics 101 discriminators through voltage limiters which limited the discriminator inputs to $\lesssim 0.7$ V. One output of each discriminator went to a neutron counter latch. The neutron counters were grouped into two banks, the "odd" counters, N_1, N_3, N_5, etc. and the "even" counters, N_2, N_4, etc. The neutron counter part of the trigger was satisfied if the upper end of any odd counter was in coincidence with the lower end of any odd counter (not necessarily the same counter), or similarly for the even counters. Since the logic for even and for odd counters was independent, it was possible to have a count in both an odd counter and an even counter and not lose any information on the event. If there was a count in more than one counter in a bank, however, the timing and pulse-height information in that bank was lost.

The signals from the eighteen photomultipliers on the anticounters were summed and brought into anticoincidence with the signals from the three proton counters. The output of the $P\bar{A}$ coincidence, with P_1 timing, was used to start the neutron time-of-flight time-to-digital converters (TDC's or "digitimes"). The outputs of the N^{down} fanouts were used to start the digitimes for up-minus-down timing. The outputs of the $N^{\mathrm{up}}N^{\mathrm{down}}$ coincidence circuits, with N^{up} timing, were used to stop the up-minus-down digitimes and the neutron time-of-flight digitimes.

An event consisted of a count in all three proton counters, no counts in any of the anticounters, and a count in one or more neutron counters. A signal from the event coincidence $P\bar{A}N_i^{\mathrm{up}}N_j^{\mathrm{down}}$ triggered the spark chambers; enabled the digital electronics, including the neutron counter latches, digitimes, and pulse area ADC's; initiated the reading of the data into the computer system; gated off the fast elec-

Table 2
Amount of data taken

	Target full		Target empty	
	18 kG	12 kG	18 kG	12 kG
number of runs	91	40	29	11
number of monitor counts (millions)	6241	2846	1299	515
number of triggers (thousands)	222	108	28	12
number of events surviving all cuts	16107	7391	137	59
Total events surviving all cuts	23498		196	

tronics for the duration of the read-out cycle; and started a delay gate of 25 msec to allow the spark chambers to recover.

Not shown in the figure are 16 TSI scalers, which scaled a variety of coincidences and single rates; the beam gate, and a gate generated by the upstream Čerenkov counter to turn off the electronics when the instantaneous beam level exceeded a preset level.

The computer system, supplied by the Brookhaven On-Line Data Facility, consisted of a Varian 4096 word X 36 bit memory and the necessary control logic to read the wire chamber data, to write the data on magnetic tape, and to transfer it to a PDP-10 computer via a data link. Preliminary analysis and checks on the performance of the equipment were performed by the PDP-10 in a time-sharing mode.

3.6. Data taking procedure

As indicated above, data were taken at two different magnet settings, 18.00 and 12.22 kG (central field). For each magnet setting, runs were taken with a full and with an empty target. The usual procedure was to take 3 or 4 runs of 1 to 4 hours each with the target full and then to take one run with the target empty. After several such sets, the magnet field was changed. Table 2 gives the amount of data taken under various conditions.

Several times a day, special runs were made to check the performance of the neutron counters, spark chambers, proton counters, and anticounters. Among the special runs were the following:

(a) Timing and performance checks of the neutron and proton counters were made by pulsing the Pek lamps mounted on the centers of the neutron counters and on the proton counters.

(b) The gain of each neutron counter was checked and adjusted at least once a day using a beta source.

(c) Each individual anticounter was placed in coincidence with the first proton counter, P_1, and ratio $P_1 A_i / P_1$ checked.

4. Data analysis

In this section we present a discussion of the off-line data analysis, done on the Princeton IBM 360/91 computer. The analysis consisted of the following procedure. Each proton track through the spectrometer system was reconstructed and the vector momentum of the proton was calculated. The flight time and the scattering angles of each neutron were calculated from the neutron arm information. Since the vector momenta of both particles in the final state, as well as the direction of the incident neutron, are known, there are three constraints on the kinematics of each event. These three constraints were used as follows. With the assumption that the event was elastic, the measured proton vector momentum was used to calculate the expected neutron angles and flight time. These calculated * parameters were compared with the measured * ones and loose cuts were made on the three differences. Those events which survived all three cuts were taken as the elastic sample. The number of elastic events as a function of t and p_{lab} was divided by the acceptance of the apparatus (from a Monte Carlo calculation) to obtain relative cross sections. A separate measurement of the neutron beam flux was used to normalize the cross sections.

4.1. Track reconstruction

The first stage of the analysis consisted of reading the raw data tapes, converting the spark coordinates into proton trajectories through the magnet, and writing the partially analyzed events on a secondary data tape.

The coordinate system used in all the analysis programs is shown in fig. 8. The coordinate system was a right-handed system with its origin at the center of the hydrogen target. The positive z-axis pointed down the beam line, the positive y-axis pointed directly downward, and the positive x-axis pointed to the right as one looked downstream. The laboratory scattering angles of the proton and the neutron, θ_p and θ_n, were measured with respect to the positive z-axis. The azimuthal angles of the proton and the neutron, ϕ_p and ϕ_n, were defined as the angles between the positive x-axis and the projections of the proton and neutron trajectories onto the x–y plane.

The raw data tapes were read and the spark coordinates for each of the magnetostrictive delay lines ("wands") were examined. The wand was checked for fiducials out of tolerance, noise before the first fiducial, and no second fiducial (unless there were two sparks). (It should be noted that these problems were rare, occurring in less than 0.5% of the triggers.) To minimize the effects of drifts, a new value for the fiducial reading was calculated every 50 events. There were no measurable drifts in most of the wands; in two wands the drift over the course of the experiment was 4 counts, corresponding to approximately 1 mm. The position of each spark along a

* The "measured" values of the neutron angles and time of flight are those measured by the neutron counters; the "calculated" values are those calculated from the proton spark chamber information.

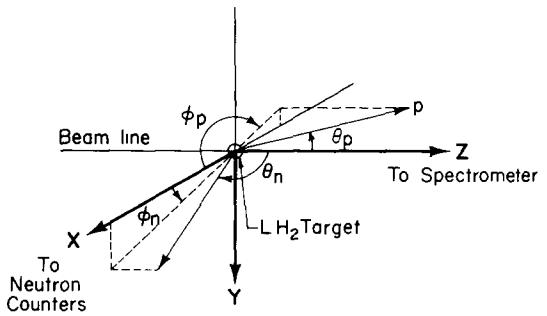

Fig. 8. Coordinate system used in the data analysis. The y-axis is down.

wand was calculated from the scaler readings and the known spacing between fiducials. At least one spark was required in each of the four pairs of chambers; otherwise the event was considered to be an accidental trigger and the event was rejected. Approximately 50% of the triggers were eliminated for this reason. Since the chambers were approximately 98% efficient and there were twice as many chambers as necessary, $< 2\%$ of the good events were eliminated in this step.

Using the surveyed positions of the center wires of each chamber the x, y and z coordinates of all possible sparks (including "ghosts" *) were calculated. Ghosts were eliminated whenever possible by comparing the spark coordinates in the two chambers of a set. On each side of the magnet all possible track segments containing 4, 3 or 2 sparks were found. Each track was fit to a straight line. A spark was included in a track if it fell within 6 mm of the line defined by two other sparks in the track.

After all possible track segments on each side of the magnet were found, the front tracks were projected upstream to the target and downstream to the magnet aperture; those tracks missing the target by more than 5 mm or the magnet aperture by more than 15 mm were eliminated. The rear tracks were projected upstream to the magnet aperture and those tracks missing the aperture were eliminated. Both front and rear tracks were then projected to the center of the magnet. The two tracks were required to lie within $\Delta x = 20$ mm and $\Delta y = 20$ mm of each other. The difference in y slope, dy/dz, between the two lines was required to be less than 0.02, and the change in x slope, dx/dz, was required to be of the proper polarity for a positively charged particle.

Approximately 30% of the triggers survived the above cuts. Of these, 90% had one complete trajectory through the spectrometer, 9% had two tracks, and 1% had three or more tracks. Information on the fitted tracks (including multiple solutions)

* Ghosts are false spark coordinate pairs which arise when there are two or more sparks in a chamber. In the case of two sparks at positions (x_1, y_1) and (x_2, y_2), there would be ghosts at positions (x_1, y_2) and (x_2, y_1).

Table 3
Number of events eliminated by the cuts (target full runs only)

	Number eliminated (thousands)	Remaining events (thousands)
Proton arm		
		330 (triggers)
Too few sparks	156	174
Track segment in front of magnet misses target	13	161
Track segment in front of magnet misses magnet aperture	2	159
Track segment in rear of magnet misses magnet aperture	5	154
$y_{front}-y_{rear}$ at magnet center too large	35	119
$x_{front}-x_{rear}$ at magnet center too large	19	100
$(dy/dz)_{front}-(dy/dz)_{rear}$ at magnet center too large	0.2	100
$(dx/dz)_{front}-(dx/dz)_{rear}$ at magnet center too large	0.2	100
Neutron arm		
Too many neutron counters	3.5	96.5
No complete neutron counters	1.5	95.0
$\Delta\theta$ too large	41.0	54.0
$\Delta\Phi$ too large	21.5	32.5
ΔTOF too large	7.5	25.0
$p_{lab} < 8$ GeV/c or $p_{lab} > 29$ GeV/c	1.5	23.5 (elastics)

was written on a secondary data tape along with all the neutron counter data for each event. All 1.1×10^5 events fit on one 2 400 foot tape, written at 1 600 bpi.

Table 3 lists the number of events eliminated by the various cuts, including the cuts described below.

A modified version of the track reconstruction program was used to calculate the efficiency of each spark chamber. The runs were divided into three groups in order to study the time dependence of the efficiencies. Only those events with a complete track through the whole spectrometer system and with three or more sparks in the track segment on the side in question were examined. As a function of position, the program counted the number of times a track passed through a given chamber without producing a spark. The inefficiency was defined as (number of misses) divided by (number of misses + number of hits). The inefficiency of the spark chamber system as a whole was

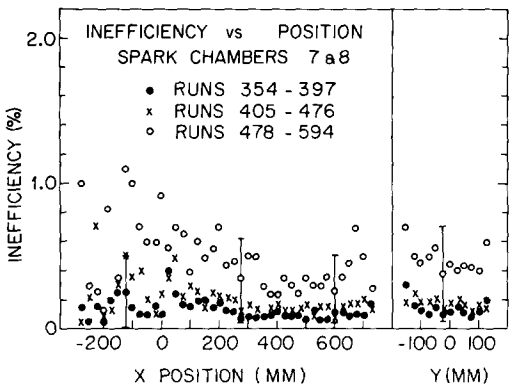

Fig. 9. Spark chamber inefficiencies for a typical pair of chambers.

$$I = I_1 I_2 + I_3 I_4 + I_5 I_6 + I_7 I_8 \,.$$

where I_i is the inefficiency of chamber i, and $I_i I_{i+1}$ is the inefficiency of the chamber pair $(i, i+1)$. A plot of inefficiency *versus* position for a typical spark chamber pair is shown in fig. 9. The inefficiency increased with time for several of the chambers.

Despite the time and position dependence of the efficiencies of some of the chambers, the efficiency of the system as a whole was high and rather constant, because there were twice as many chambers as necessary. Under the worst conditions, the efficiency varied by 1% as a function of position. The overall efficiency for the three sets of runs was 99%, 98.5% and 98%. For purposes of normalization, the efficiency of the spark chamber system was taken to be 98.5% ± 1.5%.

In order to determine the exact relationship between the scaler readings of the second fiducial and of the center wire (which was surveyed and served as a position reference), a set of runs was made in which the center wire of each plane was pulsed. On the average, the center wire had a scaler reading which was 3.6 scaler units more than half the second fiducial scaler reading. Uncertainties due to varying pulse sizes were ± 2 units, or ± 0.5 mm.

A series of "straight through" runs were made using the beam to trigger the system in the usual way, but with the analyzing magnet turned off. If the chamber alignment was correct, all tracks should have been straight lines. The analysis program required at least three sparks (out of a possible four) in a track on each side of the magnet and then looked at the intersections of the front and rear tracks at the center of the magnet. The results for the front track minus the rear track are shown in fig. 10. Central values were $\Delta x = 0.5$ mm, $\Delta y = 1.5$ mm, $\Delta(\mathrm{d}x/\mathrm{d}z) = -0.05$ mrad, and $\Delta(\mathrm{d}y/\mathrm{d}z) = 0.25$ mrad. The differences in x and y are reasonable, since the surveying was good to at best ± 1 mm and possibly only ± 1.5 mm in the first set of chambers. The error in bending angle was sufficiently small that no correction was necessary when calculating the proton momentum in normal runs.

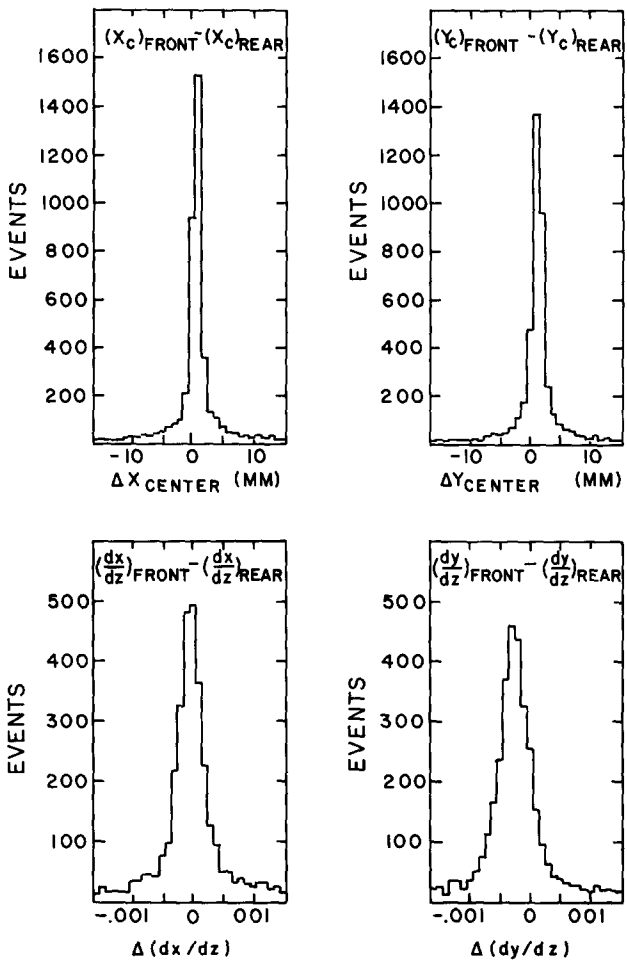

Fig. 10. Comparison of the measured front and rear proton trajectories (magnet off).

Chamber alignment was also checked during normal (magnet on) runs by examining the residuals for each chamber. A residual is the difference (x or y) between the measured position of a spark in a chamber and the fitted line from all the sparks on a track (for tracks with a spark in all four chambers on a given side of the magnet). Residuals in x varied from 0.1 mm to 0.6 mm; residuals in y varied from 0.2 mm to 1.3 mm. These residuals are of approximately the same size as the values of Δx and Δy obtained from the "straight through" runs and indicate that there were small errors ($\sim$ 1 mm) in the placement of some of the chambers. These errors were corrected by the methods described below.

4.2. Kinematic reconstruction and selection of the elastic events

In the second stage of the analysis, the kinematics of each event was calculated from the information on the secondary data tape. A comparison of the information from the proton and the neutron arms of the experiment indicated whether each event was elastic. Various small corrections were applied to the data, as discussed at the end of this section.

The first step was to determine which neutron counter fired and whether the neutron counter information was analyzable. The latches for the two ends of each counter were examined, and the following criteria were used to choose the proper counter

(a) If both ends of only one counter fired, that counter was chosen.

(b) If both ends of two counters fired (an odd and an even), the event was accepted, but the counter was chosen later, based on the proton information.

(c) If more than one counter in a bank fired, that bank was rejected, since the timing and pulse height information for that bank was destroyed.

(d) If both ends of several counters fired, but either the even or the odd bank had only one counter firing, that bank was chosen.

(e) If there were no complete counters firing (both ends), the event was rejected.

If there were one or more useable neutron counters, the proton information was then examined. If there was more than one possible proton trajectory, each was treated separately. The positions and angles of the tracks on the two sides of the magnet were used to calculate the momentum of the proton,

$$p = \frac{e}{c} \frac{\int \boldsymbol{B} \cdot \mathrm{d}\boldsymbol{l}}{\cos\psi(\sin\alpha_\mathrm{f} - \sin\alpha_\mathrm{i})} ,$$

where ψ was the angle between the proton trajectory and the x–z plane; the angles α_i and α_f, measured in the x–z plane, were the initial and final angles of the trajectory with respect to the z-axis ($\tan\alpha_\mathrm{i} = (\mathrm{d}x/\mathrm{d}z)_\mathrm{front}$, $\tan\alpha_\mathrm{f} = (\mathrm{d}x/\mathrm{d}z)_\mathrm{rear}$); and $\boldsymbol{B}(x, y, z)$ was the magnetic field. The field integral $\int \boldsymbol{B} \cdot \mathrm{d}\boldsymbol{l}$ was approximated by its value along the line $x = y = 0$, and small corrections (typically less than 0.1%) were made to the momentum calculation based on a knowledge of $\Delta B/B_0$ (B_0 was the central field) as a function of x and y. Under the assumption that the event was elastic, the proton vector momentum was used to calculate the four-momentum transfer squared t, the neutron scattering angle θ_n, the neutron azimuthal angle ϕ_n, the neutron time of flight TOF, and the momentum of the incident neutron p_lab.

The neutron counter information was used to calculate θ_n, ϕ_n, and TOF. If there were two acceptable counters, as in case (b) above, these quantities were calculated for both counters. There was one acceptable counter in 91% of the events and two acceptable counters in 4% of the events. In the other 5% of the events, there were either no complete neutron counters or too many counters.

The azimuthal angle of the neutron was $\tan\phi_\mathrm{n} = (y - y_\mathrm{t})/(x - x_\mathrm{t})$, where x and y were the coordinates of the neutron interaction in the neutron counter, and x_t and

y_t were the coordinates of the interaction in the hydrogen target (obtained by projecting the proton back to the $z = 0$ plane in the target). The x coordinate in the counter was the perpendicular distance between the beam line and the center of the counter. The y coordinate was determined from the timing difference between the upper and lower photomultipliers of the counter:

$$y = \tfrac{1}{2}c(\tau - \tau_0) ,$$

where τ was the timing difference for the event, τ_0 was the timing difference corresponding to $y = 0$ and c was the speed of light in the counter.

The scattering angle θ_n of the neutron was the average angle of the neutron counter (see table 1), with a small correction based on the value of y. Since part of counter N_1 was outside the allowed angular range for elastic events, a smaller value of θ_n, corresponding to a point $\frac{1}{4}$ of the distance across the face of the counter, was used for that counter.

The neutron time of flight TOF was determined by the timing difference between P_1 and the upper neutron counter photomultiplier, with corrections for the distance of P_1 from the target, the position of the interaction in the neutron counter, and the neutron counter pulse height. The time of flight was

$$\mathrm{TOF} = (T - T_0) + (\mathrm{TOF})_{\mathrm{av}} - \tfrac{1}{2}(\tau - \tau_0) ,$$

where T was the measured timing difference between P_1 and N^{up} for the event; T_0 was the measured timing difference corresponding to an "average" event from the light pulsers; $(\mathrm{TOF})_{\mathrm{av}}$ was the time delay between the light pulser on P_1 and the light pulser on the center of the neutron counter for the "average" event (see table 1); and τ and τ_0 were the up minus down timing differences as defined above.

For some events there was more than one possible proton track or more than one possible neutron counter. For those events, the best proton track and neutron counter were chosen by comparing the values of θ_n, ϕ_n, and TOF calculated from the proton information with the values measured by the neutron arm, for each possible combination of proton and neutron solutions. A χ^2 value was calculated, based on $\Delta\theta_n$, $\Delta\phi_n$, and ΔTOF, and on estimated widths for these distributions; the set of proton and neutron solutions with the lowest χ^2 was chosen.

Elastic events were selected by the following procedure. The values of θ_n, ϕ_n, and TOF measured by the neutron counters were compared with the values calculated from the proton vector momentum assuming an elastic event. Fig. 11 shows histograms of the differences in the three quantities, for counters N_1 through N_{15} combined. Histograms such as these were examined for each counter separately, and appropriate widths for loose cuts were determined. The three cuts were applied to each event, and those events surviving all three cuts were taken as the elastic sample. This sample contained some backgrounds.

Fig. 12 shows the distributions of fig. 11 where the data in each distribution has been cut on the other two quantities. In order to determine the background as a

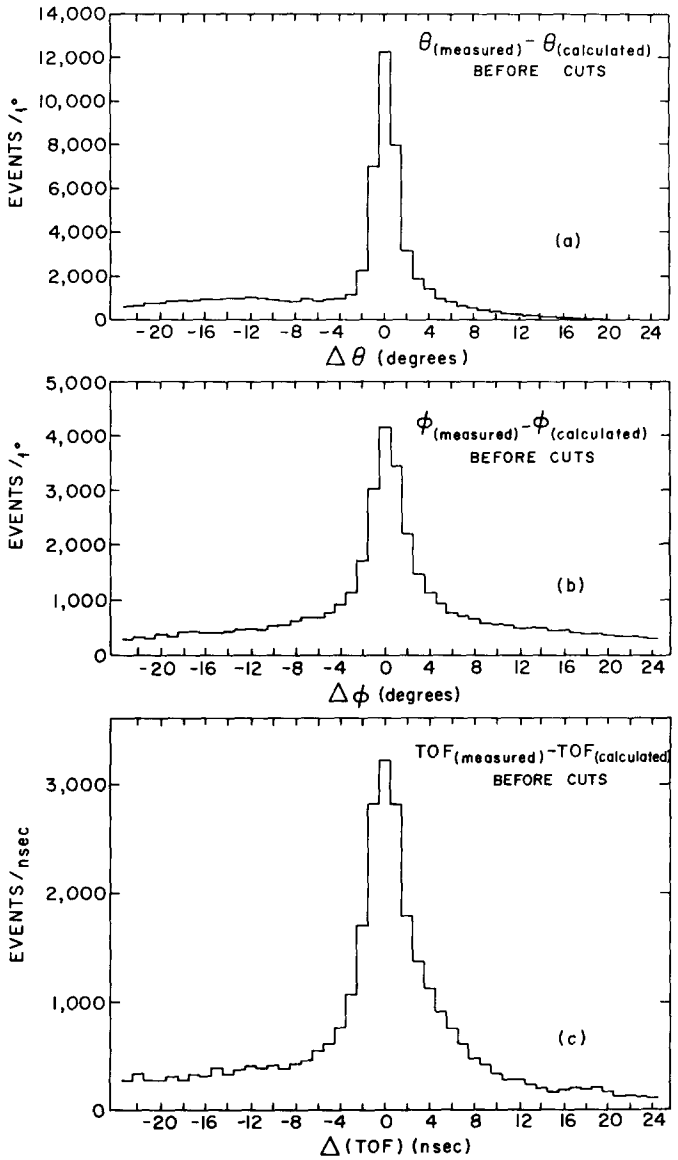

Fig. 11. $\Delta\theta$, $\Delta\Phi$, ΔTOF distribution before cuts.

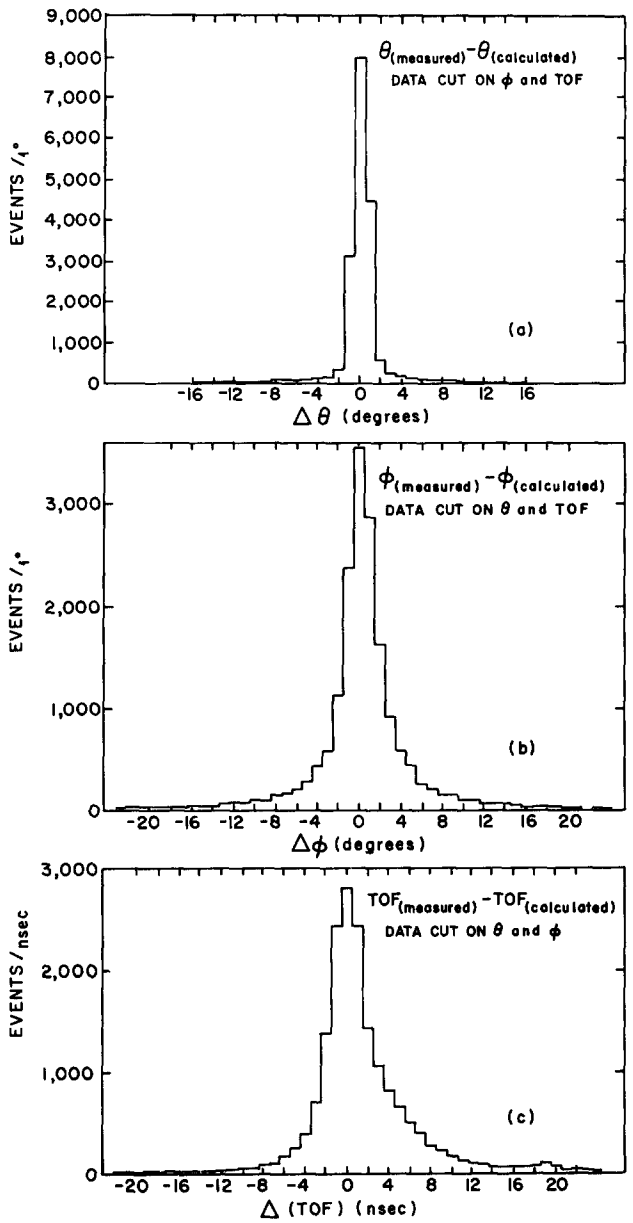

Fig. 12. $\Delta\theta$, $\Delta\Phi$, ΔTOF distributions after cuts on the other distributions.

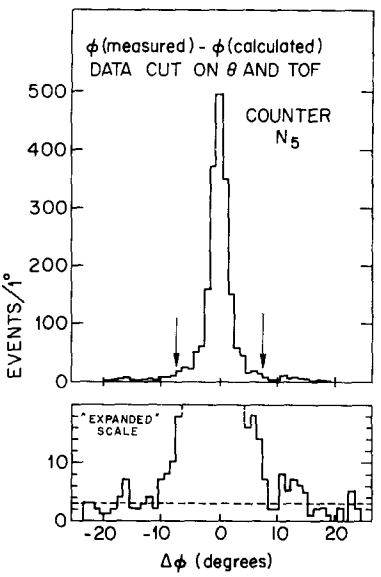

Fig. 13. Background determination for a typical counter.

function of t, distributions such as these were examined for each individual counter and for several ranges of t. Backgrounds were determined using the coplanarity ($\Delta\phi$) distribution, since it had the largest backgrounds.

Fig. 13 shows the background determination for a typical neutron counter, N_5. The cuts on $\Delta\phi$ are indicated by arrows. A flat background was assumed, with a value equal to the average number of counts per bin outside the cuts. The background for N_5 is indicated by a dashed line; the number of background counts inside the cuts is approximately 2.5% of the total events inside the cuts.

Fig. 14 shows the backgrounds as a function of t. The backgrounds are largest at small $|t|$ because the slow neutrons corresponding to small $|t|$ require longer timing gates and higher neutron counter gains than the neutrons at larger $|t|$. Backgrounds increase at large $|t|$ ($\gtrsim 0.6$ (GeV/c)^2) because the number of inelastics increases as the angle with respect to the beam decreases and because the fast neutrons corresponding to large $|t|$ are difficult to separate from the inelastics by time-of-flight measurements.

During the kinematic reconstruction several small corrections were made for the following systematic effects: (i) drifts in the up-minus-down timing over the course of the experiment; (ii) a dependence of the measured neutron times of flight on neutron counter pulse height; (iii) errors in the assumed lengths of some of the cables used as delays in the light pulser runs; (iv) small errors in the assumed positions of the spark chambers. These corrections will now be discussed in more detail.

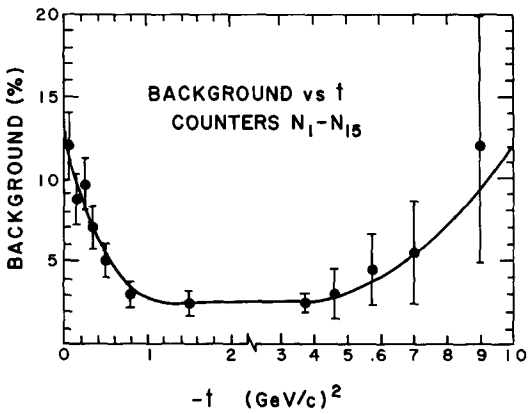

Fig. 14. Background *versus t*.

4.2.1. Up-minus-down timing

As described previously, a light pulser was placed at the center of each neutron counter. The up-down timing difference τ_0 corresponding to an interaction at the center of the counter was determined by pulsing the lamp. The values for τ_0 determined by this method were found to change slowly with time. Typical drifts over the several months of the experiment were 0.5 to 1 nsec. Corrections were made for these drifts.

After corrections were made for timing drifts, the dependence of up-minus-down timing (for the Pek lamp runs) on pulse height was examined. Only N_1 had any significant dependence, and pulse-height corrections to up-minus-down timing were made only for that counter.

4.2.2. TOF versus pulse height

Neutron times of flight were measured relative to the Pek lamp runs described previously. The light pulsers had too small a pulse-height range to provide a direct calibration of the pulse-height corrections to TOF. It was therefore necessary to use the n–p scattering data to determine these corrections.

Pulse-height corrections to the time of flight were determined by looking at the distributions in TOF (measured by the neutron counters) minus TOF (calculated from the proton vector momentum) as a function of pulse height.

Since TOF (calculated), which depends only on information from the proton arm, is independent of neutron pulse height, the quantity ΔTOF will have the same pulse-height dependence as TOF (measured). We can therefore determine the pulse-height corrections to TOF (measured) by looking at the dependence of ΔTOF on pulse height. Fig. 15 shows ΔTOF *versus* pulse height in various pulse area intervals (note that the pulse area is plotted on a logarithmic scale). The arrows show the average pulse height for the Pek lamp run which served as the time-of-flight reference.

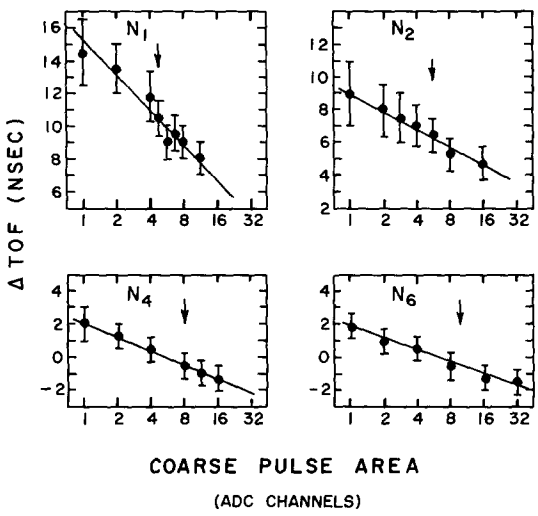

Fig. 15. ΔTOF *versus* pulse area.

For counters N_3 through N_{15}, ΔTOF was approximately zero at the reference pulse height, as expected; for counters N_1 and N_2, however, there was a discrepancy of several nanoseconds. The slopes of the ΔTOF *versus* pulse-height curves were approximately the same for counters N_3 through N_{15}; for counters N_1 and N_2, however, the slopes were somewhat steeper.

The fact that counters N_1 and N_2 have non-zero values of ΔTOF at the reference pulse height has two possible explanations. One explanation is that there is a systematic timing error in the first two counters, probably due to an error in the length of the cables used in the Pek lamp timing runs. Another explanation is there is an error in the value of TOF (calculated) because of a small spark chamber misalignment. These two possibilities were investigated, as described in subsects. 4.2.3 and 4.2.4 below.

Pulse-height corrections were made to each measured time of flight, based on the difference between the pulse area of the event and the reference pulse area for the neutron counter. As shown in fig. 15 the corrections were approximately linear in the logarithm of the pulse area.

4.2.3. Cable errors

Because of their length and the fact that they attenuated the Pek lamp pulses by approximately 30%, the timing cables used on N_1 and N_2 were subject to errors of approximately 2 nsec. It was possible to check for systematic errors in the cables by comparing the measured times of flight in two adjacent counters for events with the same calculated times of flight (calculated from the proton information). It was found that counters N_1 and N_2 gave the same measured times of flight in their re-

gions of overlap, while counter N_3 gave measured times of flight which were approximately 2 nsec shorter than those of N_2 (for the same calculated TOF). On the basis of this evidence, 2 nsec were subtracted from all the measured times of flight for counters N_1 and N_2.

4.2.4. Spark chamber position errors

The runs with the spectrometer magnet turned off indicated that errors in the bending angle of the proton were negligible. However, due to surveying uncertainties, it was still possible for the chambers to be misaligned in such a way that there could be a systematic error in the scattering angle θ_p. Data from elastic n–p scattering events were used to determine the size of the angular correction (if any) to be made to the proton trajectory in front of the magnet.

The correction to be made to θ_p was determined in the following way. A systematic error in θ_p will cause an error in TOF (calculated). This error in TOF (calculated) will increase as the incident neutron momentum increases, since, for a given neutron TOF, the proton scattering angle becomes smaller as p_{lab} increases. By examining the dependence of TOF (calculated) on p_{lab}, for fixed TOF (measured), it is possible to calculate the size of the systematic error in θ_p.

The dependence of TOF (calculated) on p_{lab} was examined for several values of TOF (measured) in counters N_1 and N_2. The value of the correction to θ_p determined in this way was 0.2 mrad. When this correction and that of subsect. 4.2.3 were applied to the data, the ΔTOF *versus* pulse area distributions for N_1 and N_2 were centered approximately around zero and had the same slope as the distributions for counters N_3–N_{15}. This correction, which is of approximately the same size as the angular resolution of the spectrometer, had a negligible effect on the shape of the angular distributions.

4.3. Monte Carlo

The acceptance of the apparatus as a function of the incident neutron momentum p_{lab} and the square of the four-momentum transfer t was calculated using a Monte Carlo computer program simulating the geometry of the apparatus. The target interaction point, the incident neutron momentum, the azimuthal angle of the interaction, and the four-momentum transfer squared were randomly chosen. The proton and neutron were then followed through the system, and those events were eliminated where one of the particles was outside the solid angle of the apparatus. A weight was assigned to each surviving event, depending on the efficiency of the neutron counter. The probability that each recoil neutron would reach a neutron counter without interacting with the material between the liquid hydrogen target and the neutron counter was calculated using standard tables of neutron-nuclei total cross sections [55]. Each event was weighted by this probability, which was typically 90 to 99%, depending on the energy of the neutron. All important information on each surviving event was written on magnetic tape. 1.3×10^6 attempts were made with

the full magnetic field (18 kG) and 7×10^5 attempts with the reduced field (12 kG), of which approximately 25% survived.

The magnetic tape was then read and such effects as multiple Coulomb scattering and measurement uncertainties were included. The Monte Carlo output was divided into bins of p_{lab} and t, and the average acceptance in each bin was determined. The acceptance was defined as: Acceptance (p, t) = (weighted number of surviving Monte Carlo events in a given p and t interval)/(number of attempts into that interval).

Typical values of the acceptance were 1 to 2%.

4.4. Normalization

The absolute normalization was done as follows:

(a) The number of incident neutrons per monitor count was measured using a total absorption spectrometer, described below.

(b) The shape of the neutron spectrum was determined from a separate experiment, described below. This information was combined with that of part (a) to get the number of neutrons per monitor count in each interval of incident neutron momentum.

(c) The absolute cross sections were found by combining the neutron flux measurements, the Monte Carlo acceptance calculations, and the data on the number of events as function of p_{lab} and t.

Various kinds of corrections were made to the cross sections. The differential cross sections are given by the following formula:

$$\frac{d\sigma}{dt}(p, t) = \frac{\text{events}\,(p, t)}{\text{acceptance}\,(p, t)} \; \frac{1}{\text{protons} \cdot \text{neutrons}\,(p)} \; ,$$

where events is the number of events in the t and p_{lab} interval; acceptance is the average acceptance in the t and p_{lab} interval; neutrons is the number of neutrons incident on the liquid hydrogen target in the given p_{lab} interval; protons is the number of protons in the target per unit area of the neutron beam.

The following corrections were applied to the cross sections. Most of these corrections have been described previously.

(a) Background subtractions of 2.5% to 13% were made.

(b) The cross sections were increased by 1.5% to correct for spark chamber inefficiencies.

(c) A target empty subtraction of 1.5% was made.

(d) Some good events were lost because there were extra neutron counters in the trigger which destroyed the timing and pulse height information. A correction of 3.3% was made for this rate effect.

(e) Due to the high counting rates in the anticounters, approximately 5% of the good events were vetoed. A correction was made for this effect.

Cross sections were calculated separately for runs with the magnetic field at 18 kG and at 12 kG. There were no systematic differences in the cross sections meas-

ured with the two different fields. The final cross sections are a weighted average of the two cross sections.

4.5. Integral neutron flux

The integral neutron flux as a function of the monitor counting rate was measured using a total absorption spectrometer (TAS) located approximately 91 m downstream of the liquid hydrogen target. The TAS consisted of 13 iron plates, 56 cm × 82 cm × 3.8 cm thick, interleaved with 14 sheets of plastic scintillator, 56 cm × 82 cm × 0.65 cm thick. The scintillators were grouped into two sets of seven, each set viewed by a 56 AVP photomultiplier. The outputs of the two photomultipliers were added passively to give a pulse height which was roughly proportional to the energy of the neutron. A more detailed description of the TAS can be found elsewhere [56].

The neutron detection efficiency of the TAS was calculated using a measured value of 1140 mb for the total cross section for neutrons on iron [56]. Since approximately $\frac{1}{3}$ of the total cross section is elastic at these energies, only $\frac{2}{3}$ of the total cross section contributes to processes leading to the production of charged particles which can be detected in the scintillator. The calculated efficiency was 96% ± 3%. The TAS was approximately 100% efficient in detecting gammas.

During the flux measurement, the instantaneous counting rate in the TAS was approximately 500 kHz, with accidentals of 5 to 10%. A series of measurements at different beam intensities was used to extrapolate to zero beam intensity. A small correction (2%) was made for gamma contamination of the beam.

The final value for the integral number of neutrons per monitor count was

$$\text{neutrons/monitor} = 32.6 \pm 1.8 ,$$

where the uncertainty of approximately 5% comes from a 4% uncertainty in gamma contamination during this measurement, a 3% uncertainty in the efficiency of the TAS, and a 1% uncertainty in extrapolating to zero beam intensity.

4.6. Neutron momentum spectrum

The momentum spectrum of incident neutrons was determined by observing the charged particles produced in the diffraction dissociation of neutrons off carbon nuclei

$$n + C \rightarrow (p\pi^-) + C .$$

At sufficiently small momentum transfers to the carbon nucleus, the nucleus can be assumed to remain in the ground state. In that case the neutron momentum can be calculated from a knowledge of the momenta of the p and the π^-. The experimental procedures are described elsewhere [57].

The above reaction is one of a class of "quasi-elastic" reactions in which the cross

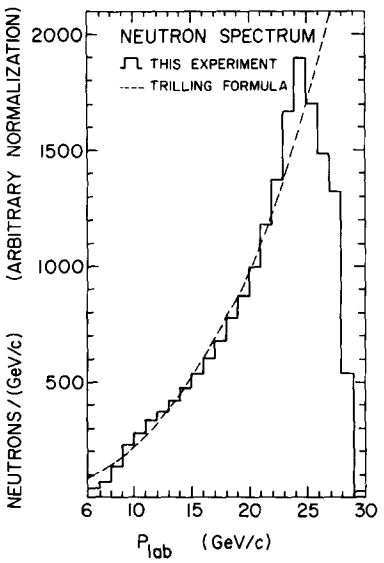

Fig. 16. Neutron spectrum.

section is expected to be essentially independent of energy [58]. Measurements of similar processes give cross sections which are essentially constant between 10 and 30 GeV/c [58–61].

Fig. 16 shows the neutron spectrum for ($p\pi^-$) masses $m_{p\pi^-}$ between 1.1 GeV and 1.35 GeV and for four-momentum transfers to the nucleus $|t'| < 0.02$ (GeV/c)^2. Uncertainties in the measured spectral shape, based on statistics and on a comparison of spectra for different intervals of $m_{p\pi^-}$ range from ± 3% at 24 GeV/c to ± 10% at 10 GeV/c. Uncertainties in the measured spectral shape due to lack of knowledge of the exact p_{lab} dependence of the diffraction dissociation cross section are approximately ± 10% at 10 GeV/c and are negligible near 24 GeV/c, the peak of the spectrum.

The broken line in fig. 16 is the Trilling formula [62] for the production of protons in a target at 0°. The proton spectrum is expected to be similar in shape to the neutron spectrum far from the kinematic limit [63].

5. Presentation and discussion of results

5.1. Cross sections and errors

The cross sections measured in this experiment are shown in figs. 17 through 25 and are tabulated in tables 4 through 12. The data were divided into 9 intervals of in-

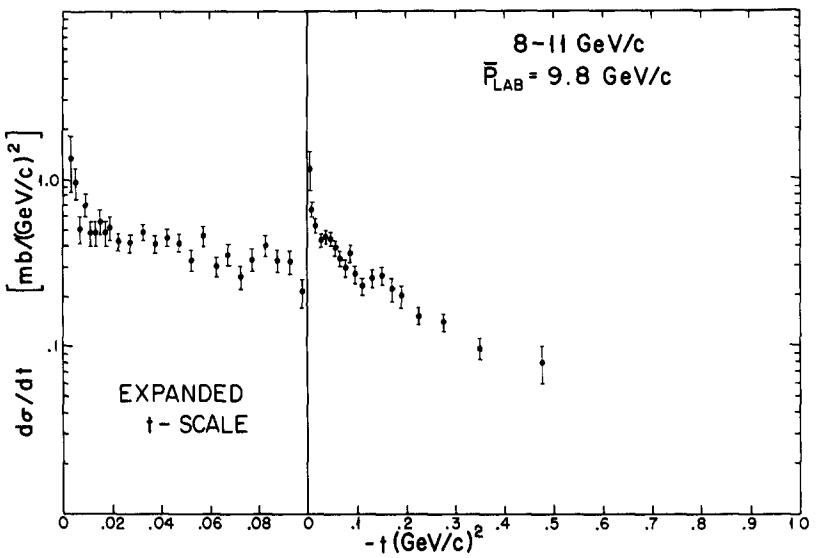

Fig. 17. np → pn differential cross section, 8–11 GeV/*c*.

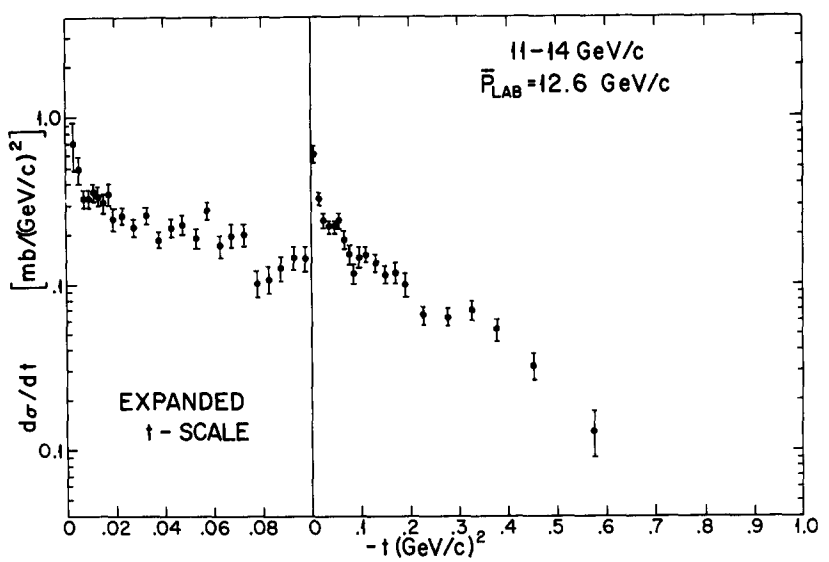

Fig. 18. np → pn differential cross section, 11–14 GeV/*c*.

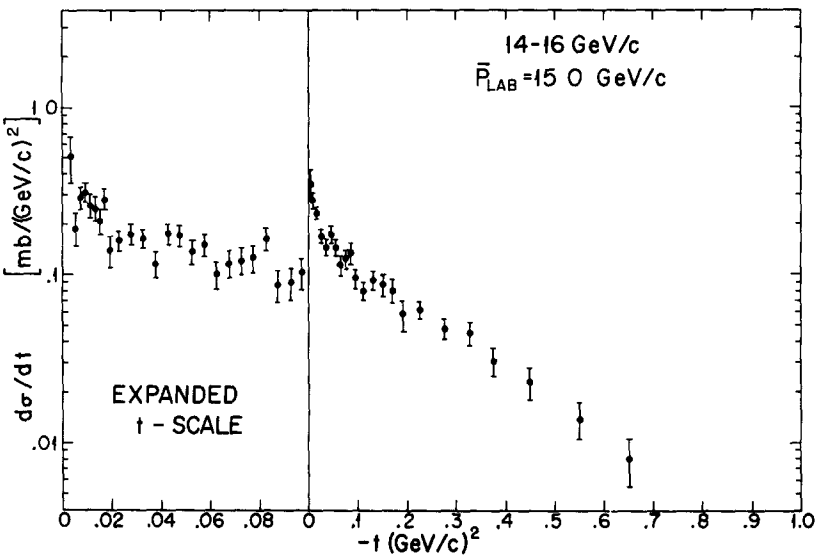

Fig. 19. np → pn differential cross section, 14–16 GeV/c.

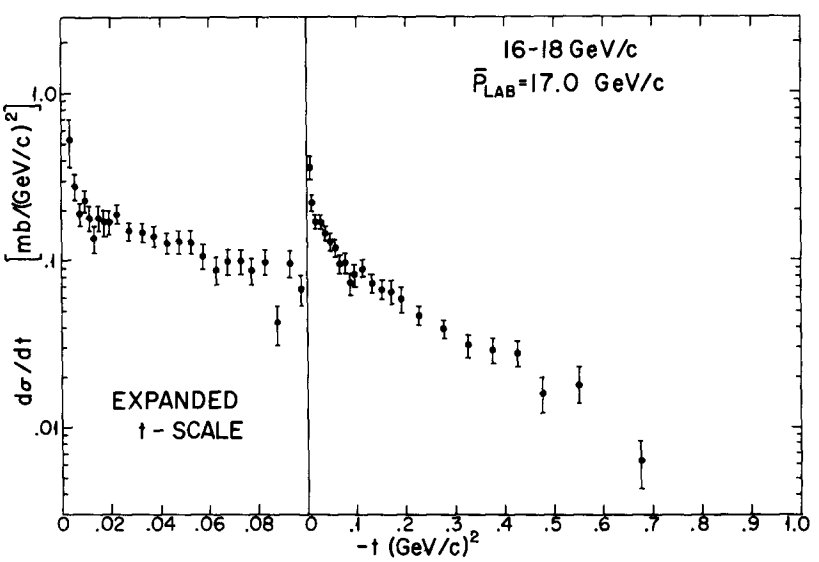

Fig. 20. np → pn differential cross section, 16–18 GeV/c.

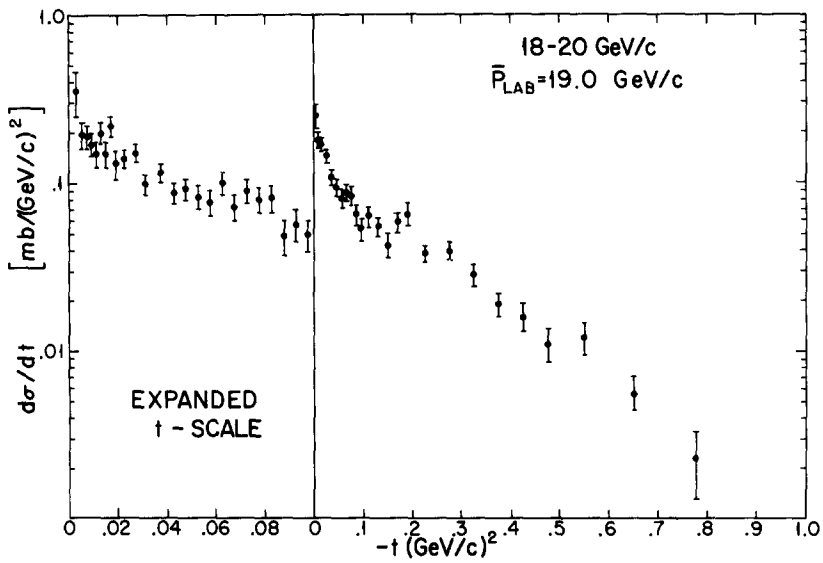

Fig. 21. np → pn differential cross section, 18–20 GeV/c.

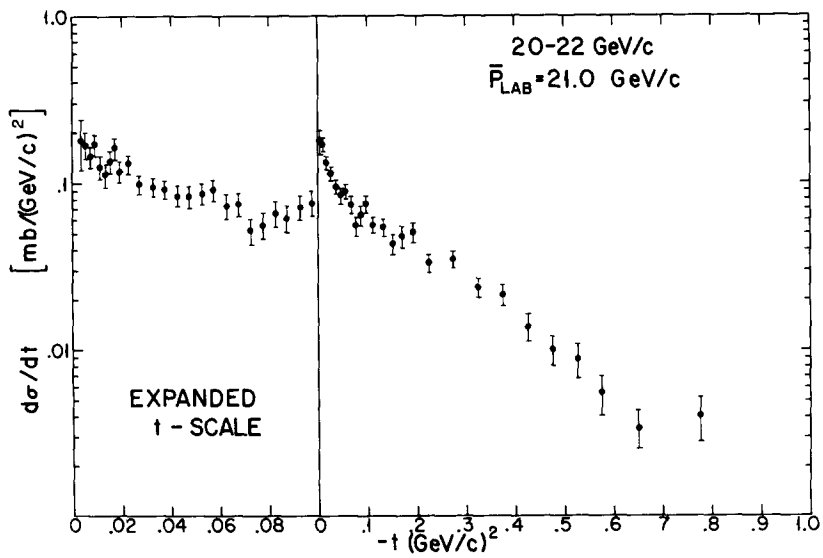

Fig. 22. np → pn differential cross section, 20–22 GeV/c.

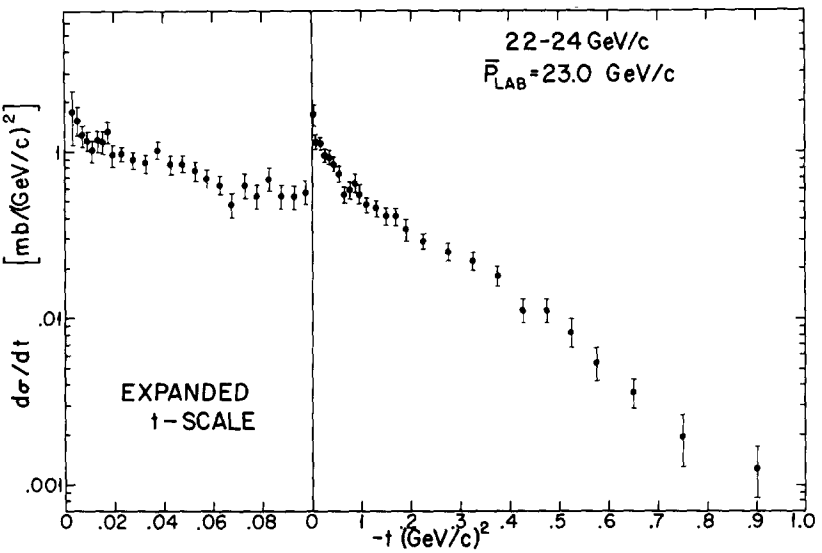

Fig. 23. np → pn differential cross section, 22–24 GeV/c.

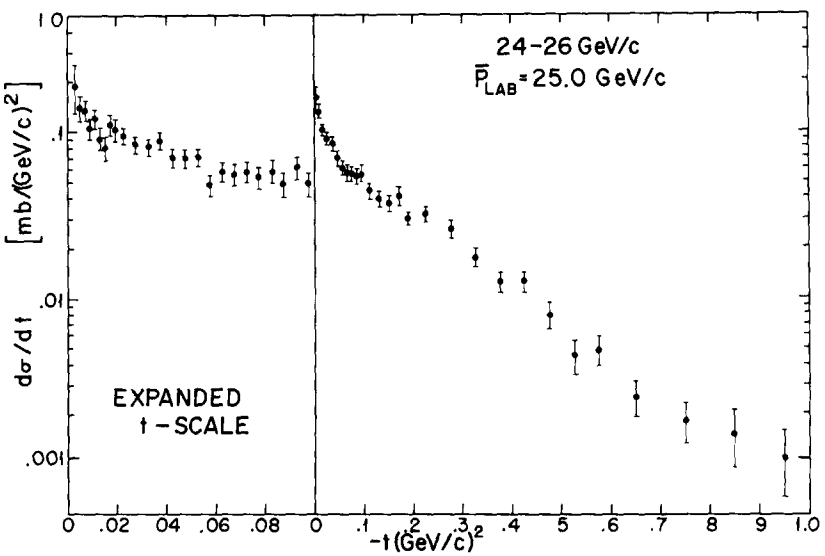

Fig. 24. np → pn differential cross section, 24–26 GeV/c.

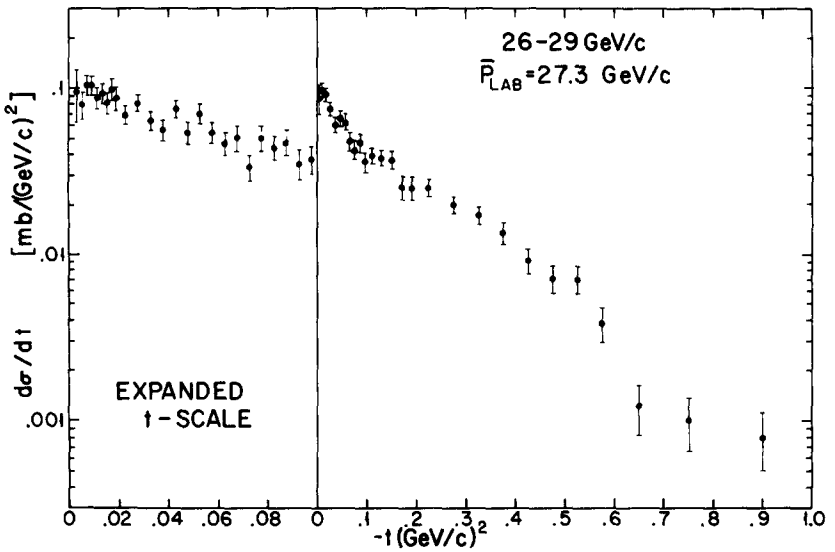

Fig. 25. np → pn differential cross section, 26–29 GeV/c.

cident neutron momentum, with approximately the same number of events in each interval. The errors shown include statistical errors and all systematic errors except uncertainties in the neutron flux. The relative systematic errors are the following:

(a) uncertainties in the background subtraction: ± 0.5 to ± 1.5%;

(b) uncertainties in the position dependence of the spark chamber efficiencies: ± 1.5%;

(c) uncertainties in the measured neutron counter efficiencies: ± 6% over most of the t range (0.006 to 1.0 (GeV/c)^2); ± 10% from 0.004 to 0.006 (GeV/c)^2; ± 30% from 0.002 to 0.004 (GeV/c)^2.

In addition to the relative errors shown in the figures, there are uncertainties which affect the absolute normalization of the cross sections but do not affect the shape of the cross sections as a function of t. The absolute systematic errors are the following:

(a) uncertainties in the measured spectral shape due to statistical errors and differences in spectra for different $m_{p\pi}$ intervals: ± 3% to ± 10%;

(b) uncertainty in the spectral shape in assuming that the diffraction dissociation cross section was independent of incident neutron momentum: ± 1% at 24 GeV/c to ± 10% at 10 GeV/c *;

(c) uncertainty in the integrated beam flux: ± 5%.

* We emphasize that even if there is a significant momentum dependence in the diffraction dissociation cross section, it will have very little effect on our absolute normalization between 18 and 26 GeV/c, near the peak in the neutron spectrum.

Table 4
np → pn differential cross section, 8–11 GeV/c

$\|t\|$ $[(\text{GeV}/c)^2]$	$d\sigma/dt$ $[\text{mb}/(\text{GeV}/c)^2]$	Error	$\|t\|$ $[(\text{GeV}/c)^2]$	$d\sigma/dt$ $[\text{mb}/(\text{GeV}/c)^2]$	Error
0.003	1.3400	0.4810	0.110	0.2330	0.0260
0.005	0.9740	0.2120	0.130	0.2540	0.0290
0.007	0.5080	0.0930	0.150	0.2660	0.0350
0.009	0.7020	0.1100	0.170	0.2210	0.0340
0.011	0.4790	0.0830	0.190	0.2010	0.0310
0.013	0.4800	0.0820	0.225	0.1510	0.0180
0.015	0.5650	0.0880	0.275	0.1400	0.0180
0.017	0.4780	0.0800	0.350	0.0969	0.0129
0.019	0.5190	0.0810	0.475	0.0789	0.0209
0.022	0.4310	0.0490			
0.027	0.4160	0.0480			
0.032	0.4870	0.0540			
0.037	0.4130	0.0490			
0.042	0.4490	0.0530			
0.047	0.4240	0.0520			
0.052	0.3270	0.0450			
0.057	0.4560	0.0560			
0.063	0.3010	0.0430			
0.067	0.3640	0.0500			
0.072	0.2580	0.0410			
0.077	0.3330	0.0490			
0.082	0.3970	0.0550			
0.087	0.3300	0.0490			
0.092	0.3200	0.0490			
0.097	0.2130	0.0390			

Average incident neutron momentum = 9.8 GeV/c.
Number of events = 2462.
Absolute normalization uncertainty = ± 15.8%.

Table 5
np → pn differential cross section, 11–14 GeV/c

$\|t\|$ $[(\text{GeV}/c)^2]$	$d\sigma/dt$ $[\text{mb}/(\text{GeV}/c)^2]$	Error	$\|t\|$ $[(\text{GeV}/c)^2]$	$d\sigma/dt$ $[\text{mb}/(\text{GeV}/c)^2]$	Error
0.003	0.7150	0.2300	0.110	0.1490	0.0150
0.005	0.4890	0.0850	0.130	0.1340	0.0150
0.007	0.3280	0.0440	0.150	0.1140	0.0140
0.009	0.3290	0.0430	0.170	0.1160	0.0160
0.011	0.3610	0.0450	0.190	0.0983	0.0155
0.013	0.3400	0.0450	0.225	0.0651	0.0080
0.015	0.3060	0.0420	0.275	0.0630	0.0082
0.017	0.3510	0.0490	0.325	0.0698	0.0092
0.019	0.2490	0.0390	0.375	0.0533	0.0084
0.022	0.2610	0.0280	0.450	0.0319	0.0059
0.027	0.2230	0.0250	0.575	0.0129	0.0039
0.032	0.2620	0.0290			
0.037	0.1840	0.0230			
0.042	0.2160	0.0260			
0.047	0.2310	0.0280			
0.052	0.1930	0.0260			
0.057	0.2820	0.0340			
0.063	0.1720	0.0250			
0.067	0.1960	0.0270			
0.072	0.1970	0.0270			
0.077	0.1020	0.0190			
0.082	0.1070	0.0190			
0.087	0.1260	0.0210			
0.092	0.1460	0.0230			
0.097	0.1420	0.0240			

Average incident neutron momentum = 12.6 GeV/c.
Number of events = 2887.
Absolute normalization uncertainty = ± 10.2%.

Table 6
np → pn differential cross section, 14–16 GeV/c

$\|t\|$ [(GeV/c)^2]	dσ/dt [mb/(GeV/c)^2]	Error	$\|t\|$ [(GeV/c)^2]	dσ/dt [mb/(GeV/c)^2]	Error
0.003	0.5140	0.1690	0.110	0.0803	0.0105
0.005	0.1860	0.0400	0.130	0.0932	0.0118
0.007	0.2870	0.0450	0.150	0.0873	0.0122
0.009	0.3070	0.0430	0.170	0.0811	0.0131
0.011	0.2630	0.0390	0.190	0.0590	0.0116
0.013	0.2500	0.0390	0.225	0.0621	0.0077
0.015	0.2070	0.0340	0.275	0.0482	0.0069
0.017	0.2810	0.0440	0.325	0.0447	0.0069
0.019	0.1410	0.0280	0.375	0.0306	0.0057
0.022	0.1610	0.0210	0.450	0.0229	0.0049
0.027	0.1740	0.0220	0.550	0.0139	0.0034
0.032	0.1640	0.0220	0.650	0.0079	0.0026
0.037	0.1160	0.0180			
0.042	0.1740	0.0240			
0.047	0.1720	0.0250			
0.052	0.1370	0.0220			
0.057	0.1480	0.0230			
0.063	0.1010	0.0180			
0.067	0.1170	0.0210			
0.072	0.1220	0.0220			
0.077	0.1250	0.0220			
0.082	0.1630	0.0260			
0.087	0.0871	0.0187			
0.092	0.0903	0.0194			
0.097	0.1030	0.0210			

Average incident neutron momentum = 15.0 GeV/c.
Number of events = 1966.
Absolute normalization uncertainty = ± 8.7%.

Table 7
np → pn differential cross section, 16–18 GeV/c

$\|t\|$ [(GeV/c)^2]	dσ/dt [mb/(GeV/c)^2]	Error	$\|t\|$ [(GeV/c)^2]	dσ/dt [mb/(GeV/c)^2]	Error
0.003	0.5320	0.1750	0.110	0.0893	0.0105
0.005	0.2790	0.0530	0.130	0.0734	0.0095
0.007	0.1930	0.0300	0.150	0.0668	0.0093
0.009	0.2340	0.0340	0.170	0.0656	0.0103
0.011	0.1810	0.0280	0.190	0.0590	0.0104
0.013	0.1360	0.0240	0.225	0.0468	0.0057
0.015	0.1770	0.0280	0.275	0.0393	0.0052
0.017	0.1690	0.0290	0.325	0.0313	0.0047
0.019	0.1680	0.0280	0.375	0.0293	0.0048
0.022	0.1890	0.0220	0.425	0.0277	0.0050
0.027	0.1510	0.0180	0.475	0.0157	0.0037
0.032	0.1480	0.0190	0.550	0.0179	0.0049
0.037	0.1400	0.0190	0.675	0.0063	0.0020
0.042	0.1270	0.0180			
0.047	0.1310	0.0190			
0.052	0.1280	0.0190			
0.057	0.1060	0.0170			
0.063	0.0880	0.0160			
0.067	0.0991	0.0175			
0.072	0.1000	0.0170			
0.077	0.0873	0.0164			
0.082	0.0998	0.0179			
0.087	0.0429	0.0115			
0.092	0.0962	0.0179			
0.097	0.0671	0.0146			

Average incident neutron momentum = 17.0 GeV/c.
Number of events = 2112.
Absolute normalization uncertainty = ± 8.0%.

Table 8
np → pn differential cross section, 18–20 GeV/c

$\|t\|$ [(GeV/c)^2]	$d\sigma/dt$ [mb/(GeV/c)^2]	Error	$\|t\|$ [(GeV/c)^2]	$d\sigma/dt$ [mb/(GeV/c)^2]	Error
0.003	0.3550	0.1180	0.110	0.0637	0.0074
0.005	0.1930	0.0370	0.130	0.0554	0.0071
0.007	0.1870	0.0270	0.150	0.0416	0.0062
0.009	0.1670	0.0250	0.170	0.0577	0.0084
0.011	0.1470	0.0230	0.190	0.0655	0.0098
0.013	0.1960	0.0280	0.225	0.0383	0.0046
0.015	0.1490	0.0240	0.275	0.0393	0.0047
0.017	0.2180	0.0320	0.325	0.0285	0.0039
0.019	0.1320	0.0230	0.375	0.0192	0.0031
0.022	0.1380.	0.0160	0.425	0.0157	0.0031
0.027	0.1490	0.0170	0.475	0.0110	0.0025
0.032	0.0982	0.0132	0.550	0.0119	0.0024
0.037	0.1160	0.0150	0.650	0.0055	0.0015
0.042	0.0873	0.0131	0.775	0.0023	0.0010
0.047	0.0926	0.0138			
0.052	0.0828	0.0135			
0.057	0.0771	0.0127			
0.063	0.1010	0.0150			
0.067	0.0721	0.0126			
0.072	0.0892	0.0151			
0.077	0.0796	0.0144			
0.082	0.0811	0.0147			
0.087	0.0480	0.0107			
0.092	0.0574	0.0120			
0.097	0.0494	0.0107			

Average incident neutron momentum = 19.0 GeV/c.
Number of events = 2290.
Absolute normalization uncertainty = ± 7.8%.

Table 9
np → pn differential cross section, 20–22 GeV/c

$\|t\|$ [(GeV/c)^2]	$d\sigma/dt$ [mb/(GeV/c)^2]	Error	$\|t\|$ [(GeV/c)^2]	$d\sigma/dt$ [mb/(GeV/c)^2]	Error
0.003	0.1820	0.0630	0.110	0.0559	0.0063
0.005	0.1680	0.0320	0.130	0.0541	0.0064
0.007	0.1420	0.0210	0.150	0.0426	0.0056
0.009	0.1690	0.0240	0.170	0.0482	0.0069
0.011	0.1250	0.0190	0.190	0.0506	0.0074
0.013	0.1120	0.0170	0.225	0.0330	0.0038
0.015	0.1360	0.0200	0.275	0.0347	0.0039
0.017	0.1620	0.0230	0.325	0.0236	0.0031
0.019	0.1170	0.0180	0.375	0.0214	0.0030
0.022	0.1270	0.0140	0.425	0.0138	0.0025
0.027	0.0991	0.0121	0.475	0.0101	0.0020
0.032	0.0954	0.0119	0.525	0.0088	0.0020
0.037	0.0917	0.0119	0.575	0.0055	0.0015
0.042	0.0850	0.0118	0.650	0.0034	0.0009
0.047	0.0828	0.0120	0.775	0.0040	0.0012
0.052	0.0865	0.0124			
0.057	0.0909	0.0135			
0.063	0.0727	0.0117			
0.067	0.0747	0.0119			
0.072	0.0523	0.0099			
0.077	0.0561	0.0101			
0.082	0.0662	0.0114			
0.087	0.0620	0.0112			
0.092	0.0720	0.0120			
0.097	0.0762	0.0127			

Average incident neutron momentum = 21.0 GeV/c.
Number of events = 2629.
Absolute normalization uncertainty = ± 7.6%.

Table 10
np → pn differential cross section, 22–24 GeV/c

$\|t\|$ $[(\mathrm{GeV}/c)^2]$	$d\sigma/dt$ $[\mathrm{mb}/(\mathrm{GeV}/c)^2]$	Error	$\|t\|$ $[(\mathrm{GeV}/c)^2]$	$d\sigma/dt$ $[\mathrm{mb}/(\mathrm{GeV}/c)^2]$	Error
0.003	0.1730	0.0590	0.110	0.0477	0.0052
0.005	0.1550	0.0270	0.130	0.0459	0.0052
0.007	0.1240	0.0170	0.150	0.0408	0.0049
0.009	0.1160	0.0150	0.170	0.0415	0.0055
0.011	0.1010	0.0140	0.190	0.0337	0.0051
0.013	0.1160	0.0160	0.225	0.0288	0.0031
0.015	0.1140	0.0160	0.275	0.0252	0.0028
0.017	0.1310	0.0190	0.325	0.0224	0.0026
0.019	0.0954	0.0142	0.375	0.0179	0.0023
0.022	0.0970	0.0104	0.425	0.0112	0.0018
0.027	0.0891	0.0101	0.475	0.0111	0.0018
0.032	0.0857	0.0101	0.525	0.0083	0.0016
0.037	0.1020	0.0120	0.575	0.0054	0.0012
0.042	0.0833	0.0102	0.650	0.0036	0.0007
0.047	0.0859	0.0105	0.750	0.0020	0.0006
0.052	0.0767	0.0101	0.900	0.0013	0.0004
0.057	0.0694	0.0096			
0.063	0.0636	0.0095			
0.067	0.0479	0.0078			
0.072	0.0636	0.0098			
0.077	0.0541	0.0089			
0.082	0.0698	0.0104			
0.087	0.0544	0.0089			
0.092	0.0543	0.0088			
0.097	0.0570	0.0093			

Average incident neutron momentum = 23.0 GeV/c.
Number of events = 3190.
Absolute normalization uncertainty = ± 7.6%.

Table 11
np → pn differential cross section, 24–26 GeV/c

$\|t\|$ $[(\mathrm{GeV}/c)^2]$	$d\sigma/dt$ $[\mathrm{mb}/(\mathrm{GeV}/c)^2]$	Error	$\|t\|$ $[(\mathrm{GeV}/c)^2]$	$d\sigma/dt$ $[\mathrm{mb}/(\mathrm{GeV}/c)^2]$	Error
0.003	0.1900	0.0610	0.110	0.0441	0.0047
0.005	0.1420	0.0250	0.130	0.0391	0.0044
0.007	0.1350	0.0180	0.150	0.0374	0.0044
0.009	0.1050	0.0140	0.170	0.0408	0.0052
0.011	0.1210	0.0160	0.190	0.0300	0.0045
0.013	0.0914	0.0129	0.225	0.0320	0.0032
0.015	0.0815	0.0124	0.275	0.0263	0.0028
0.017	0.1110	0.0160	0.325	0.0175	0.0021
0.019	0.1040	0.0150	0.375	0.0123	0.0017
0.022	0.0959	0.0101	0.425	0.0125	0.0018
0.027	0.0844	0.0092	0.475	0.0080	0.0014
0.032	0.0828	0.0094	0.525	0.0044	0.0010
0.037	0.0892	0.0102	0.575	0.0048	0.0010
0.042	0.0699	0.0085	0.650	0.0025	0.0006
0.047	0.0692	0.0087	0.750	0.0018	0.0005
0.052	0.0719	0.0093	0.850	0.0015	0.0006
0.057	0.0478	0.0071	0.950	0.0011	0.0005
0.063	0.0580	0.0082			
0.067	0.0548	0.0081			
0.072	0.0577	0.0087			
0.077	0.0535	0.0083			
0.082	0.0582	0.0088			
0.087	0.0486	0.0078			
0.092	0.0615	0.0093			
0.097	0.0492	0.0080			

Average incident neutron momentum = 25.0 GeV/c.
Number of events = 3397.
Absolute normalization uncertainty = ± 7.6%.

Table 12
np → pn differential cross section, 26–29 GeV/c

$\|t\|$ $[(\mathrm{GeV}/c)^2]$	$d\sigma/dt$ $[\mathrm{mb}/(\mathrm{GeV}/c)^2]$	Error	$\|t\|$ $[(\mathrm{GeV}/c)^2]$	$d\sigma/dt$ $[\mathrm{mb}/(\mathrm{GeV}/c)^2]$	Error
0.003	0.0957	0.0332	0.110	0.0395	0.0043
0.005	0.0790	0.0151	0.130	0.0379	0.0044
0.007	0.1030	0.0140	0.150	0.0369	0.0045
0.009	0.1030	0.0140	0.170	0.0247	0.0037
0.011	0.0870	0.0124	0.190	0.0248	0.0040
0.013	0.0932	0.0131	0.225	0.0251	0.0028
0.015	0.0820	0.0126	0.275	0.0200	0.0023
0.017	0.0995	0.0142	0.325	0.0172	0.0021
0.019	0.0877	0.0137	0.375	0.0135	0.0019
0.022	0.0686	0.0080	0.425	0.0092	0.0015
0.027	0.0809	0.0093	0.475	0.0070	0.0013
0.032	0.0640	0.0080	0.525	0.0071	0.0014
0.037	0.0558	0.0075	0.575	0.0038	0.0009
0.042	0.0747	0.0091	0.650	0.0012	0.0004
0.047	0.0542	0.0077	0.750	0.0010	0.0004
0.052	0.0699	0.0093	0.900	0.0008	0.0003
0.057	0.0541	0.0081			
0.063	0.0465	0.0073			
0.067	0.0499	0.0078			
0.072	0.0336	0.0063			
0.077	0.0496	0.0080			
0.082	0.0440	0.0073			
0.087	0.0471	0.0078			
0.092	0.0350	0.0066			
0.097	0.0374	0.0070			

Average incident neutron momentum = 27.3 GeV/c.
Number of events = 2653.
Absolute normalization uncertainty = ± 8.6%.

Uncertainties in the spark chamber efficiencies were included in the relative errors above.

The overall normalization errors are indicated on the tables. They vary from ± 16% at 10 GeV/c to ± 8% at 25 GeV/c.

5.2. *Observations*

We can make the following general observations about the cross sections:

(a) The shape of the cross sections agrees very well with the measurements of Miller et al. [10, 11] and Engler et al. [12].

(b) The absolute normalizations agree, within errors, with those of Miller et al. and Engler et al. (see fig. 29).

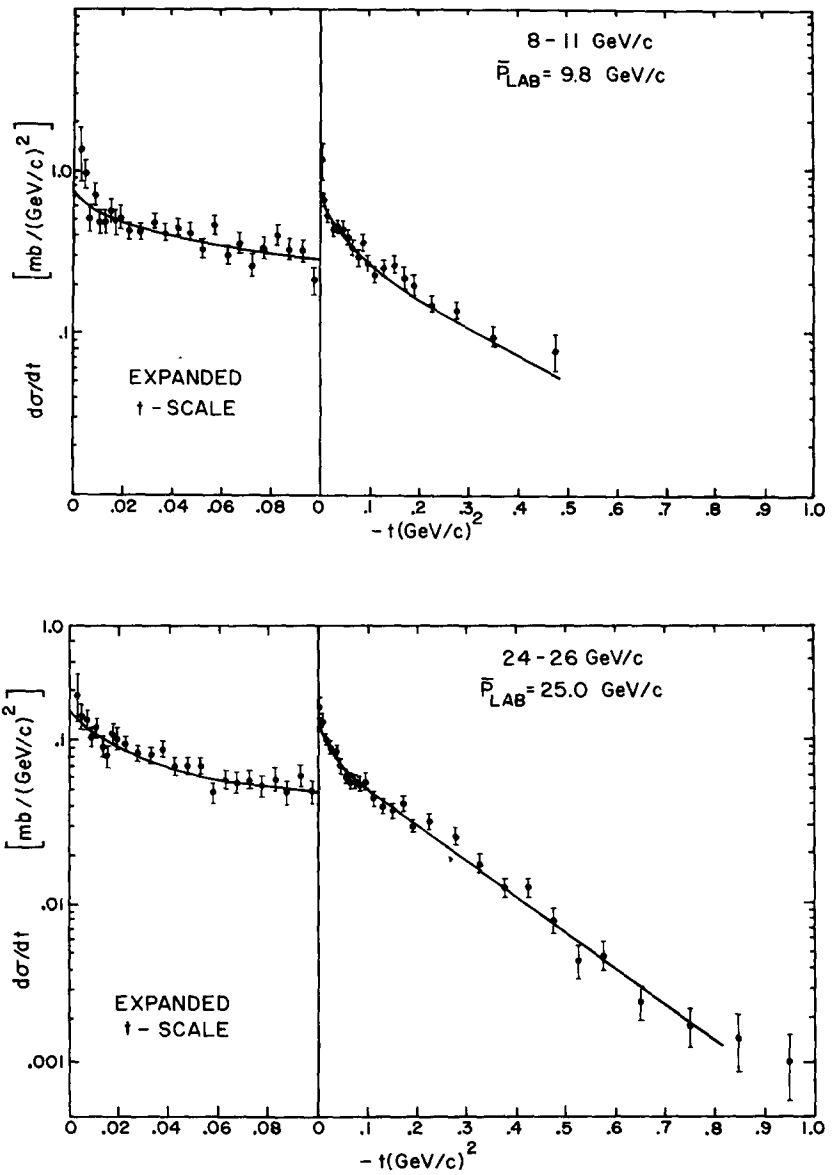

Fig. 26. Two exponential fits to two typical cross sections.

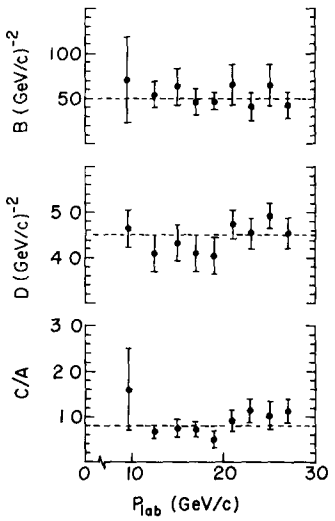

Fig. 27. Parameters from the two exponential fit.

(c) The shape of the cross sections appears to be independent of energy. In particular, the sharp peak persists to at least 29 GeV/c.

(d) There may be some structure in the cross sections near $-t = 0.10$ (GeV/c)^2.

(e) There appears to be curvature in the t distributions for $-t > 0.4$ (GeV/c)^2.

5.3. Energy dependence of the cross sections

In order to study the energy dependence of the cross sections and to compare our results with those of other experiments, we have fit our cross sections to the standard two exponential form: $d\sigma/dt = A\, e^{-B|t|} + Ce^{-D|t|}$. Since the data at large $|t|$ appear to be more complicated than this simple parametrization would imply, we have restricted the fits to $-t \leqslant 0.5$ (GeV/c)^2. Fig. 26 shows the results of such a fit for two of our cross sections. Fig. 27 shows the values of the parameters B, D and (C/A) for each region of incident neutron momentum. The values for these parameters appear to be essentially independent of momentum. The weighted average over the entire momentum interval yields

$$d\sigma/dt = f(p_{lab}) \times (e^{-(51\pm 8)|t|} + (0.8 \pm 0.1)e^{-(4.50\pm 0.15)|t|}),$$

where $f(p_{lab})$ is a function of p_{lab}. The $t = 0$ cross sections extracted from this parametrization are shown in fig. 28 and demonstrate a $p_{lab}^{-(1.81\pm 0.25)}$ dependence *.

* These values differ slightly from those of ref. [1]. The differences are due to improvements in extrapolating the measured cross sections to $t = 0$ and to improvements in the determination of the neutron spectrum.

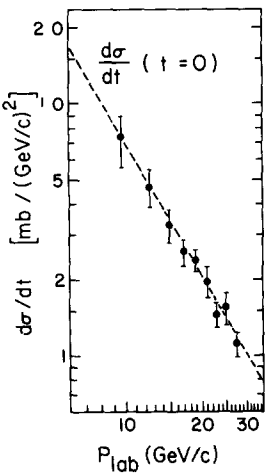

Fig. 28. Momentum dependence of $d\sigma/dt$ ($t = 0$).

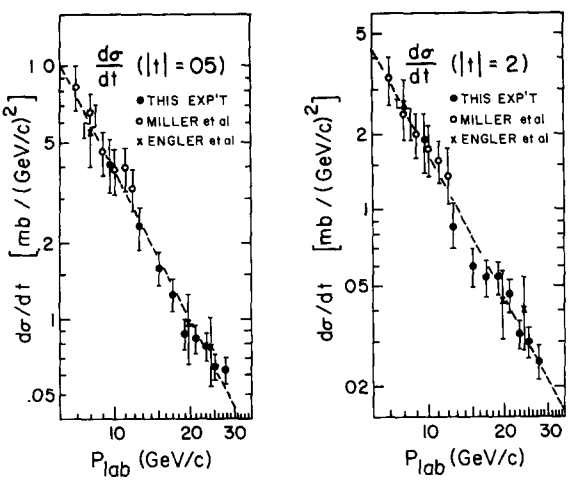

Fig. 29. Momentum dependence of $d\sigma/dt$ at $-t = 0.05$ (GeV/c)^2 and $-t = 0.2$ (GeV/c)^2.

Fig. 29 shows the momentum dependence of the cross sections at fixed t. The cross sections of Miller et al. [10, 11] and Engler et al. [12] are also plotted and agree within experimental errors with the measurements of this experiment. The cross sections at $-t = 0.05$ and $-t = 0.2$ show a momentum dependence of $p_{\text{lab}}^{-(1.75 \pm 0.25)}$ and $p_{\text{lab}}^{-(1.72 \pm 0.30)}$ respectively. When the data of Miller et al. and Engler et al. are included, the values of the exponent change to $-(1.97 \pm 0.15)$ and $-(1.89 \pm 0.20)$ respectively.

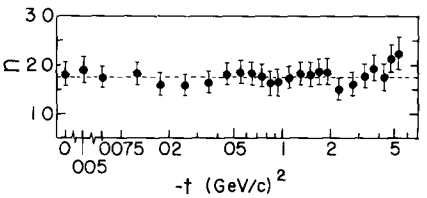

Fig. 30. n *versus* t, where $(d\sigma/dt)_{t=\text{const.}} \propto p_{\text{lab}}^{-n}$.

We have examined the momentum dependence of the cross sections at fixed t, by fitting the data to the form $d\sigma/dt = F(t)p_{\text{lab}}^{-n}$. The results of these fits are shown in fig. 30. The average value of n assuming no t dependence is 1.75 ± 0.15. The value of n is sensitive to the lowest momentum point, which has a normalization uncertainty of ± 16%. Varying the value of the 9.8 GeV/c cross section by 16% changes the average value of n by 0.1. If the Miller data are included in the fit, the average n changes to 1.95 ± 0.10.

5.4. Comparison with theory

Our data indicate that the s dependence of the n–p charge-exchange cross sections is approximately s^{-2}, for values of $-t$ between 0.0 and 0.5 (GeV/c)^2 and for

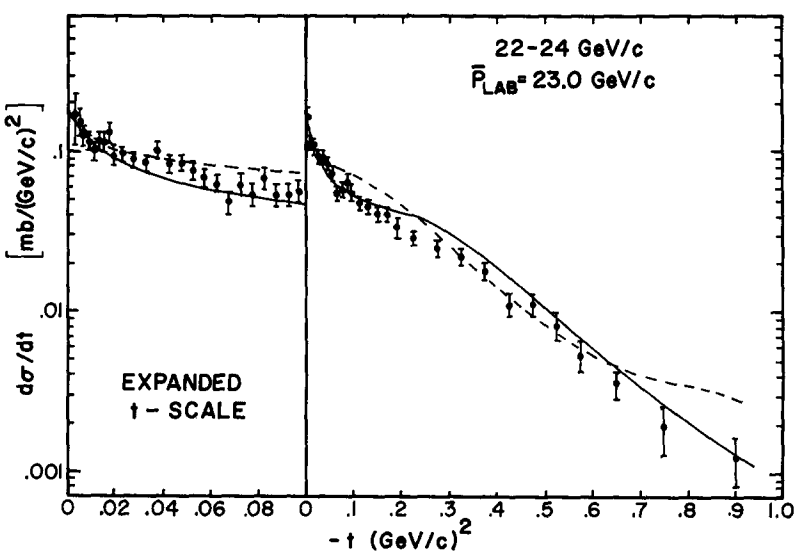

Fig. 31. Comparison of a typical cross section with models. The dashed line is the prediction of the SCRAM model (ref. [45]). The solid line is a fit with an absorption model with the pion contribution suppressed for $-t \geq 0.2$ (GeV/c)^2, (ref. [46]).

energies up to 29 GeV. In the one-Regge exchange model this is the s-dependence expected for an interaction dominated by the exchange of a single pion. There is no evidence for shrinkage of the angular distributions between 8 and 29 GeV/c.

In fig. 31 we have compared our cross sections for 22–24 GeV/c with two of the models described above. The dashed line is the prediction of the SCRAM model of Richards et al. [45]. The parameters in this model were determined by fitting data for several other reactions as well as lower energy n–p charge-exchange data. This model is able to predict the magnitude and general shape of the cross sections.

The solid line in the figure is a fit to our data done by Gotsman and Maor [46], using their absorption model with suppression of the pion contribution for $-t \geqslant 0.2$ (GeV/c)^2. They were able to fit our data rather well.

5.5. *Final remarks*

The general dependence of n–p charge exchange scattering on four-momentum transfer and energy up to 29 GeV is now fairly well known. However, there are still questions regarding details of the differential cross sections. None of the models has been able to explain all the features of the measured cross sections, and most models are inadequate at large values of $|t|$.

Two groups are preparing to study n–p charge exchange scattering at higher energies. At Serpukhov, the CERN-Serpukhov collaboration of Engler et al. is preparing to take data at energies up to 70 GeV. The Michigan State-Ohio State collaboration of Abolins et al. is setting up an experiment at the Fermi National Accelerator Laboratory to study the reaction up to 300 GeV. Perhaps with the data from the present experiment and with future data from the two higher energy experiments, better models can be constructed.

We would like to thank Tom McCorriston, Tim Toohig, Tad Dobrowolski, and Bruce Gibbard for their help during the early phases of this experiment. We would also like to thank Fred Schwarz, Bart Gibbs, Jim Pluta and Orman Haas for their technical support. The staff of the A.G.S., especially the On-Line-Data Facility, is to be thanked for their support.

References

[1] M.B. Davis, B.G. Gibbard, M.N. Kreisler, T. Dobrowolski, M.J. Longo, D.D. O'Brien and T. Toohig, Phys. Rev. Letters 29 (1972) 139.

[2] M.B. Davis, Ph.D. thesis, Princeton University, Technical report No. 4, COO-3072-14 (1972), unpublished.

[3] M.B. Davis, B.G. Gibbard, M.N. Kreisler, T. Dobrowolski, M.J. Longo, D.D. O'Brien and T. Toohig, Proc. of the 4th Int. Conf. on high-energy collisions, Oxford, p. 35, vol. 2 (1972).

[4] H. Palevsky, J.A. Moore, R.L. Stearns, H.R. Muether, R.J. Sutter, R.E. Chrien, A.P. Jain and K. Otnes, Phys. Rev. Letters 9 (1962) 509.

[5] J.L. Friedes, H. Palevsky, R.L. Stearns and R.J. Sutter, Phys. Rev. Letters 15 (1965) 38.
[6] S.T. Powell III, Elastic neutron-proton charge exchange scattering between 1.75 GeV/c and 7.20 GeV/c, University of Michigan, thesis (1970), unpublished.
[7] R.R. Larsen, Nuovo Cimento 18 (1960) 1039.
[8] G. Manning, A.G. Parham, J.D. Jafar, H.B. van der Raay, D.H. Reading, D.G. Ryan, B.D. Jones, J. Malos and N.H. Lipman, Nuovo Cimento 41A (1966) 167.
[9] R.E. Mischke, P.F. Shepard and T.J. Devlin, Phys. Rev. Letters 23 (1969) 542.
[10] E.L. Miller, M. Elfield, N.W. Reay, N.R. Stanton, M.A. Abolins, M.T. Lin and K.W. Edwards, Phys. Rev. Letters 26 (1971) 984.
[11] E.L. Miller, Ph.D. thesis, Ohio State University (1971).
[12] J. Engler, K. Horn, F. Mönnig, P. Schludecker, W. Schmidt-Parzefall, H. Schopper, P. Sievers, H. Ullrich, R. Hartung, K. Runge and Yu. Galaktionov, Phys. Letters 34B (1971) 528.
[13] R. Wilson, Ann. of Phys. 32 (1965) 193.
[14] M.A. Abolins, M.T. Lin, R.C. Ruchti, J.G. Horowitz, R.C. Kammerud, N.W. Reay, K. Reibel, N.R. Stanton, K. Edwards, D.G. Crabb and J.R. O'Fallon, Phys. Rev. Letters 30 (1973) 1183.
[15] G.F. Chew, Phys. Rev. 112 (1958) 1380.
[16] N.S. Amaglobeli and Yu.M. Kazarinov, ZhETF (USSR) 37 (1960) 1125.
[17] A. Ashmore, W.H. Range, R.T. Taylor, B.M. Townes, L. Castillejo and R.F. Peierls, Nucl. Phys. 36 (1962) 258.
[18] P. Cziffra and M.J. Moravcsik, Phys. Rev. 116 (1959) 226.
[19] R.J.N. Phillips, Phys. Letters 4 (1963) 19.
[20] I.J. Muzinich, Phys. Rev. Letters 11 (1963) 88.
[21] M.M. Islam and T.W. Preist, Phys. Rev. Letters 11 (1963) 444.
[22] M. Glück, Phys. Rev. Letters 29 (1972) 1762.
[23] R.J.N. Phillips, Phys. Rev. Letters 11 (1963) 442.
[24] D.V. Bugg, Phys. Letters 7 (1963) 365.
[25] K. Gottfried and J.D. Jackson, Nuovo Cimento 34 (1964) 735.
[26] E.M. Henley and I.J. Muzinich, Phys. Rev. 136B (1964) 1783.
[27] L. Durant and Y.T. Chiu, Phys. Rev. 137B (1965) 1530; 139B (1965) 646.
[28] G.A. Ringland and R.J.N. Phillips, Phys. Letters 12 (1964) 62.
[29] G.L. Kane, private communication.
[30] N. Byers and C.N. Yang, Phys. Rev. 142 (1966) 976,
N. Byers, Phys. Rev. 156 (1967) 1703.
[31] V.D. Barger and D.B. Cline, Phenomenological theories of high-energy scattering (Benjamin, 1969).
[32] F. Arbab and J.W. Dash, Phys. Rev. 163 (1967) 1603.
[33] A. Ahmadzadeh, Phys. Rev. 134B (1964) 633.
[34] V. Flores-Maldonado, Phys. Rev. Letters 17 (1966) 113; Phys. Rev. 155 (1967) 1773.
[35] D.V. Volkov and V.N. Gribov, ZhETF (USSR) 17 (1963) 720.
[36] R.J.N. Phillips, Nucl. Phys. B2 (1967) 394.
[37] J. Geicke and K.H. Mütter, Phys. Rev. 184 (1969) 1551.
[38] P. Finkler, Phys. Rev. D1 (1970) 1172.
[39] B.K. Pal, Phys. Rev. D1 (1970) 1405.
[40] M. Le Bellac, Phys. Letters 25B (1967) 524.
[41] K. Huang and I.J. Muzinich, Phys. Rev. 164 (1967) 1726.
[42] A.B. Kaidalov and B.M. Karnakov, Phys. Letters 29B (1969) 372.
[43] F. Henyey, G.L. Kane, J. Pumplin and M.H. Ross, Phys. Rev. 182 (1969) 1579.
[44] M. Ross, F.S. Henyey and G.L. Kane, Nucl. Phys. B23 (1970) 269.
[45] G.L. Kane, F. Henyey, D.R. Richards, M. Ross and G. Williamson, Phys. Rev. Letters 25 (1970) 1519;
D.R. Richards, Ph.D. thesis, University of Michigan (1971).

[46] E. Gotsman and U. Maor, Nucl. Phys. B46 (1972) 525.
[47] S. Chia, Phys. Rev. D5 (1972) 2316; D7 (1973) 1496.
[48] J. Engler, F. Mönnig, K. Runge and H. Schopper, Nuovo Cimento 9A (1972) 311.
[49] M. Lusignole and Y. Srivastava, Phys. Rev. Letters 28 (1972) 1348.
[50] Science Accessories Corporation, Southport, Connecticut.
[51] M. Buttram, Ph.D. thesis, Princeton University (1970), unpublished.
[52] S.C. Curran, Luminescence and the scintillation counter (Butterworths, London, 1953); J.B. Birks, The theory and practice of scintillation counting (Pergamon, 1964).
[53] A. Chastel, M.B. Davis, C.M. Hoffman, M.N. Kreisler and A.J.S. Smith, Nucl. Instr. 94 (1971) 493.
[54] Pek Labs, Inc., Sunnyvale, California.
[55] Neutron cross sections, BNL 325, supplement No. 2 (1964).
[56] T.P. McCorriston, Ph.D. thesis, University of Michigan (1972); L.W. Jones, M.J. Longo, T.P. McCorriston, E.F. Parker, S.T. Powell and M.N. Kreisler, Phys. Letters 36B (1971) 509.
[57] M.J. Longo, L.W. Jones, D.D. O'Brien, J.C. VanderVelde, M.B. Davis, B.G. Gibbard and M.N. Kreisler, Phys. Letters 36B (1971) 560; J.C. VanderVelde, L.W. Jones, M.J. Longo, D.D. O'Brien, M.B. Davis, B.G. Gibbard and M.N. Kreisler, Nucl. Phys. B45 (1972) 1; D.D. O'Brien, M.J. Longo, J.C. VanderVelde, M.B. Davis and M.N. Kreisler, Nucl. Phys. B77 (1974) 1.
[58] D.R. Morrison, Phys. Rev. 165 (1968) 1699; Phys. Letters 22 (1966) 528, 226.
[59] G. Cocconi, E. Lillethun, J.P. Scanlon, C.A. Stahlbrandt, C.C. Ting, J. Walters and A.M. Wetherell, Phys. Letters 8 (1964) 134.
[60] E.W. Anderson, E.J. Bleser, G.B. Collins, T. Fujii, J. Menes, F. Turkot, R.A. Carrigan, R.M. Edelstein, N.C. Hien, T.J. McMahon and I. Nadelhaft, Phys. Rev. Letters 16 (1966) 855.
[61] H.H. Bingham, CERN/D.Ph.II/PHYS/70-60; Proc. of Topical Seminar on interactions of elementary particles with nuclei, Trieste (1970).
[62] 200 GeV Accelerator Design Study, vol. 1, section XIII-1.3, p. XIII-6, Lawrence Radiation Laboratory, University of California (1965).
[63] J. Engler, W. Flauger, B. Gibbard, F. Mönnig, K. Pack, K. Runge and H. Schopper, 4th Int. Conf. on high-energy collisions, Oxford, April, 1972.